

Observation of period doubling and higher multiplicities in a driven single-spin system

Dhruv Deshmukh ^{1,2,*} Raúl B. González ^{3,2,†} Roberto Sailer ^{3,2,†}
Fedor Jelezko ^{3,2} Ressa S. Said ^{3,2} and Joachim Ankerhold ^{1,2}

¹*Institute for Complex Quantum Systems, Universität Ulm, Albert-Einstein-Allee 11, D-89069 Ulm, Germany.*

²*Center for Integrated Quantum Science and Technology, Albert-Einstein-Allee 11, 89081 Ulm, Germany.*

³*Institute for Quantum Optics, Universität Ulm, Albert-Einstein-Allee 11, 89081 Ulm, Germany.*

One of the prime features of quantum systems strongly driven by external time-periodic fields is the subharmonic response with integer multiples of the drive period kT_d . Here we demonstrate experimentally based on a careful theoretical analysis period doubling and higher multiplicities ($k = 2, \dots, 5$) for one of the most fundamental systems, namely, an individual spin-1/2. Realized as a nitrogen vacancy center in diamond, the particular coherence properties under ambient conditions, strong field sensitivity, and optical addressability allow to monitor coherent k -tupling oscillations over a broad set of driving parameters in the vicinity of the ideal manifolds. We verify an enhanced sensitivity within this domain which provides new means for improved sensing protocols.

Quantum systems can be controlled and manipulated when they are exposed to time-periodic external fields. While this has been both theoretically explored and experimentally implemented in a vast variety of situations over decades, the topic has gained fundamental relevance in the era of quantum technologies, for example, in the context of quantum sensing and quantum information processing. The basic ingredients are two level systems (TLS) realized with physical platforms ranging from atomic ensembles to various types of solid state devices.

The conventional scenario is the regime of weak driving where driving amplitudes are sufficiently smaller than energy level spacings of the system under consideration. In this so-called Rabi regime the system's frequency response follows the amplitude of the drive linearly which allows to design pulses, for example, for sensing protocols and qubit gate operations. Much less common though is the domain beyond, i.e. the domain of moderate to strong driving. Strongly pulsed driving has been explored in [1, 2]. For time-periodic driving theory has analyzed and predicted a wealth of emerging phenomena such as the AC-Stark effect [3], multi-photon transitions [4, 5], localization [6], and subharmonic response [7, 8]. However, corresponding experiments are challenging and progress has been achieved only in a few instances and with specially designed driving sequences for e.g. superconducting nonlinear resonators [9, 10], ensembles of atoms [11, 12], and composites of spins in solid state structures [13].

In this respect, the dynamical response of a *single* spin-1/2 driven by a strong sinusoidal field has not been systematically explored yet in experiments. Here we fill this gap and demonstrate one of the most intriguing phenomena, namely, period doubling and higher multiplicities based on a careful analysis within Floquet theory [14]. Apart from its relevance for actual quantum devices, it provides insight into fundamental processes of quantum mechanical time evolution as such, see e.g. [15]. In presence of a strong time-periodic field with period T_d , a single TLS is shown to respond with coherent oscillatory dynamics with periods of integer multiples kT_d . This occurs not merely for an expectation value of a specific observable or for a well-chosen initial state but for any initial

state, at any chosen time, and thus for any observable. By monitoring period doubling ($k = 2$) and higher multiplicities ($k = 3, 4, 5$) in the vicinity of the respective ideal drive parameters by means of a stroboscopic measurement scheme, we verify a strongly enhanced sensitivity of the TLS with respect to any perturbation which in turn may offer new avenues for sensing applications. Moreover, the particular case of period doubling allows for a very efficient state to state transfer on the Bloch sphere following a non-trivial inter-period trajectory, potentially of relevance for fast gate operations.

A pre-requisite for observing k -tupling with an individual spin is a sufficiently long coherence time. In experiments, Nitrogen-Vacancy centers in diamond (NV centers) outperform other TLS realizations thanks to their room-temperature coherence [16], their field sensitivity [17, 18], and their optical addressability. In particular, no pulse engineering is required, regular sinusoidal driving is sufficient. As prime indicator for the emergence of period doubling, we observe in the domain around the corresponding parameter manifold, characteristic superimposed low frequency oscillations with a period that tends to infinity towards this manifold. Here, as shown theoretically, the TLS of the NV becomes particularly sensitive to any residual degrees in its surrounding such as, for example, nuclear spins. Extended modeling captures all observed features very precisely and allows to systematically retrieve higher multiplicities for various initial states. This way, we establish a consistent theoretical and experimental picture of a fundamental physical phenomenon for strongly driven systems which specifically refers to the NV-center realization but conceptually applies to other platforms as well.

Theoretical background. – We consider the simplest possible paradigm, namely, a TLS with level spacing Δ_0 subject to a classical time-periodic drive with amplitude A , frequency $\omega_d = 2\pi/T_d$, and initial phase φ_0 , obeying the Hamiltonian,

$$H = \frac{\Delta_0}{2} \sigma_z + A \sin(\omega_d t + \varphi_0) \sigma_x$$

with Pauli matrices σ_x, σ_z . The general theoretical framework to analyze the quantum dynamics of such a periodically driven system is based on the Floquet theory [8, 14, 19, 20]. It implies the existence of T_d -periodic so-

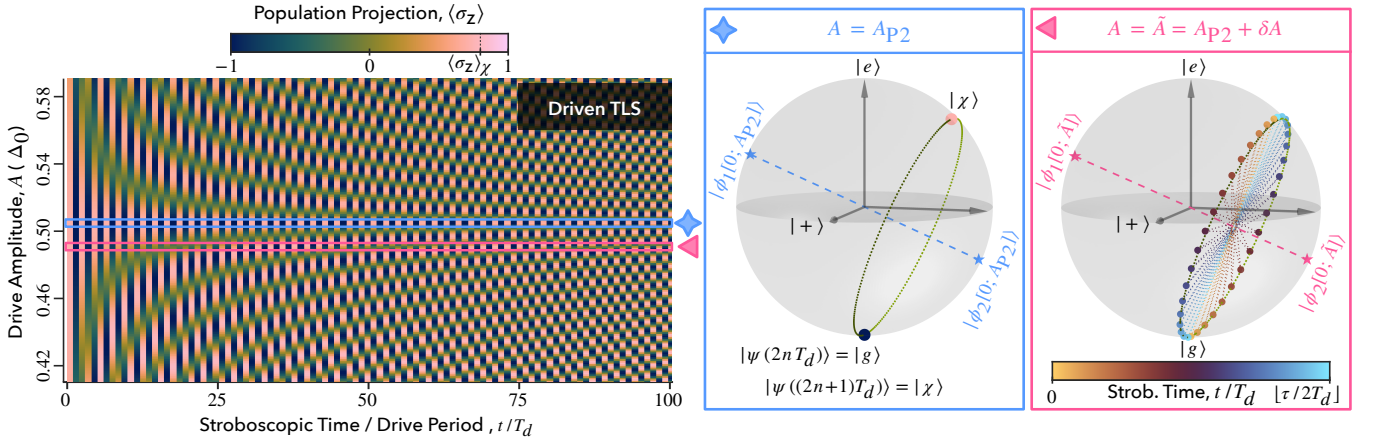


FIG. 1. Stroboscopic population dynamics of a resonantly driven spin-1/2 in multiples of the driving period T_d according to Floquet theory. The system is initialized in the ground state $|g\rangle$ and driving amplitudes A are close to the period doubling amplitude A_{P2} . Left panel: Population projection $\langle \sigma_z \rangle$ evaluated after each drive-cycle T_d . Right boxes: Dynamics on the Bloch sphere. At the amplitude A_{P2} (left, blue star) the alternating pattern of vertical blue-pink stripes shows that the projection flips between the initial value -1 and $\langle \chi | \sigma_z | \chi \rangle \simeq 0.7099$ and implies $2T_d$ -periodic revivals. On the Bloch sphere (right, blue box), this pattern corresponds to state $|g\rangle$ perpetually hopping to the state $|\chi\rangle$ and back. These states lie diametrically opposite on the circle about the associated Floquet mode axis $|\phi_1[0; A_{P2}]\rangle - |\phi_2[0; A_{P2}]\rangle$. Slightly away from the ideal amplitude, for $\tilde{A} = A_{P2} + \delta A$ (left, pink triangle), this alternating pattern is modulated. On the Bloch sphere (right, pink box) the stroboscopic trajectory lies on a circle passing through $|g\rangle$ on a plane perpendicular to a slightly shifted Floquet mode axis, $|\phi_1[0; \tilde{A}]\rangle - |\phi_2[0; \tilde{A}]\rangle$. After each $2T_d$ the stroboscopic orbit shifts slightly, returning to $|g\rangle$ only after a modulation period $\tau \propto 1/|\delta A|$.

lutions to Schrödinger's equation, namely the Floquet states $e^{-i\varepsilon_1 t/\hbar} |\phi_1(t)\rangle$ and $e^{-i\varepsilon_2 t/\hbar} |\phi_2(t)\rangle$, which serve as basis states for the quantum dynamics. Here, the quasi-energies $\varepsilon_{1,2}$ are defined modulo the drive-photon energy $\hbar\omega_d$. Using these basis states, the stroboscopic dynamics of any state $|\psi(0)\rangle$, represented in the polar coordinates (θ, η) of the associated Bloch sphere, can be written as:

$$|\psi(nT_d)\rangle = \cos\left(\frac{\theta}{2}\right) |\phi_1(0)\rangle + e^{-i2\pi n \cdot \frac{\Delta\varepsilon}{\hbar\omega_d}} e^{i\eta} \sin\left(\frac{\theta}{2}\right) |\phi_2(0)\rangle,$$

where $\Delta\varepsilon = \varepsilon_2 - \varepsilon_1$ is the quasi-energy difference. An interesting dynamical response, which we refer to as period k -tupling, occurs when $\Delta\varepsilon/\hbar\omega_d = j/k$ for some $j < k \in \mathbb{N}$. Despite the Hamiltonian and the Floquet states possessing T_d -periodicity, all of the superposition states exhibit a lower symmetry with a non-trivial $k T_d$ -periodicity. The condition of period k -tupling has been found to be fulfilled by families of (1d) manifolds $\{A_k, \omega_{d,k}\}$ on the drive-parameter $(A-\omega_d)$ space. Below, we explore in detail the k -tupling dynamics of the driven two-level system in the neighborhood of few isolated points on these manifolds for amplitudes $A \lesssim \Delta_0$ driven in tune, $\hbar\omega_d = \Delta_0$.

The transformation $|\psi(t_0)\rangle \rightarrow |\psi(nT_d + t_0)\rangle$, in the case of period k -tupling can be seen as a sequence of discrete rotations on the Bloch sphere about the Floquet mode axis by the angle $2\pi j/k$. Specifically at the period doubling amplitude A_{P2} , any state $|\psi(t_0)\rangle$ rotates by π radians about the Floquet mode axis, $|\phi_1[0; A_{P2}]\rangle - |\phi_2[0; A_{P2}]\rangle$ after each period T_d , see Fig. 1. A small deviation in the drive-amplitude $\tilde{A} = A_{P2} + \delta A$ results in a violation of the period-doubling condition, i.e. $\Delta\varepsilon/\hbar\omega_d = (1/2 + \xi)$, $|\xi| \ll 1$. The consequence of this deviation on the stroboscopic evolution is a slow rotation along a circle around the Floquet axis as shown in Fig. 1. It is this rotation which leaves a characteristic imprint on the experimental data

and serves as a proxy for the approach towards the parameter manifold for period doubling. A numerical simulation of the stroboscopic population dynamics starting from the ground state of the bare TLS, equivalent to its survival probability, is depicted in Fig. 1. It shows the population projection in the vicinity of the exact period doubling amplitude $A_{P2} \simeq 0.5042\Delta_0$ for $\hbar\omega_d = \Delta_0$. At the amplitude A_{P2} , one sees an alternating pattern of the projection values whilst for small deviations $A \neq A_{P2}$, this ideal behavior is modulated with a period τ , where τ tends to infinity in the limit $A \rightarrow A_{P2}$, as illustrated in Fig. 1.

Experimental realization. – To demonstrate this dynamical response in a physical realization, we use a single NV center – a point defect in the diamond lattice that contains a substitutional nitrogen atom and a neighboring vacancy (Fig. 2). The ground state of the NV center's electronic energy levels (3A) has a spin triplet ($S = 1$). The state with zero spin projection, $|m_S = 0\rangle$ is separated from the degenerate states $|m_S = \pm 1\rangle$ by a zero-field splitting of $\Delta_0 = 2.87$ GHz. The effective TLS, spanned by $\{|m_S = 0\rangle, |m_S = -1\rangle\}$, can be achieved through an external static magnetic field. Our experiment uses a sample with solid immersion lens for a higher photon collection efficiency and a better signal-to-noise ratio. Spin initialization and read-out are performed by a 532 nm optical laser in a home-built confocal setup. To control spin dynamics via radio-frequency fields, we utilize an arbitrary waveform generator with 0.02 ps time resolution and 10-bit voltage digitization which has $\Delta V \approx 0.5$ mV at $V_{pp} = 500$ mV. It allows for scanning through the required amplitude ranges $A \sim \Delta_0$ for observing the period tupling. Our measured NV spin coherence time, $T_2^* \approx 75 \mu\text{s}$, is over 100 times longer the periodicity $T_d = 1/\Delta_0$. For more details on the experimental details, we refer to [21].

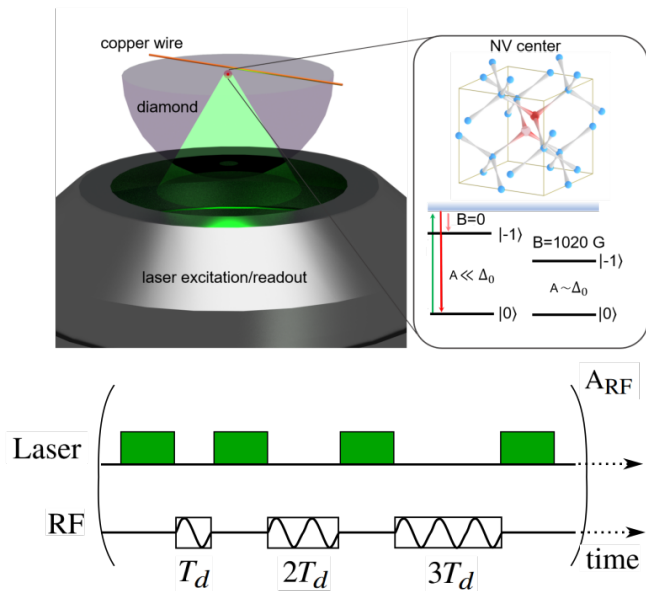


FIG. 2. Experimental realization. (a) Setup, NV center structure, and electronic energy levels. A 532 nm laser (green cone; green arrow) is used for confocal microscopy experiments with a single NV center. The spin system is coherently controlled by an RF-field via a copper wire antenna. The green laser is used to initialize the NV center into the $|m_S = 0\rangle$ spin state. The spin state is read out by monitoring the fluorescence (red arrow) with different state-dependent intensities for $|m_S = 0\rangle$ and $|m_S = -1\rangle$ (bright and dark red arrow). To reach $A \sim \Delta_0$ for observing period k -tupling close to the ground state level anti-crossing (GSLAC), a high magnetic bias with an optimal alignment is applied. (b) Driving and measurement protocol for observing period multiplicity. For each time trace, the sequence contains rectangular pulses with a fixed length $T_{\text{pulse}} = nT_d$ ($T_d \equiv 2\pi/\omega_d \simeq 1/\Delta_0$). After each RF-pulse, a laser pulse is applied, where for this sequence a multiple shot of measurements is done. By using this fixed set of parameters the RF-amplitude A is increased for each measurement cycle.

Now, to make a strong driving protocol feasible which is essential to observe period k -tupling, the spin transition must be tuned down sufficiently, i.e. in the range of $A \sim \Delta_0$. By adjusting the magnetic bias strength and orientation, this range is close to the ground state level anti-crossing (GSLAC) (Fig. 1 in [21]). In order to achieve a high measurement contrast beneficial for high-fidelity state initialization [22, 23], the field strength is set around 1020 G with an orientation aligned with the NV axis. This yields a transition between the states $|m_S = 0\rangle$ and $|m_S = -1\rangle$ of about 9.21 MHz, on which the driving and measurement protocol is implemented as shown in Fig. 2(b). The spin is initialized after $3 \mu\text{s}$ of optical pumping followed by a sequence of rectangular RF pulses with a pulse length $T_{\text{pulse}} = nT_d$ ($n \in \mathbb{N}$). For a fixed A_{RF} , the pulse length will be swept after each measurement, and the photoluminescence (PL) will be measured with the same initializing optical laser. The repetitive procedures for the various measurement times are controlled and processed by the suite QUDI [24].

Results and Discussion. – Figure 3a (bottom) shows the stroboscopically measured PL signal after every drive cycle. One

can clearly identify the characteristic period doubling pattern consisting of alternate blue and pink vertical stripes along with its modulation manifested through the green fan-like structure, as already shown in Fig. 1. As a salient feature, we extract in Fig. 3b the hyperbolic dependence of the modulation period $\tau \propto 1/|A - A_{P2}|$ on driving amplitude deviations, as predicted for the TLS. Not only does this enable us to locate the period doubling amplitude precisely but it also corroborates the scaling of quasi-energy differences with the drive amplitude in the vicinity of A_{P2} . The steep rise of the modulation period while approaching towards the amplitude A_{P2} holds the key for practical applications, owing to its high sensitivity to any residual interactions. It offers promising perspectives both for sensing external electromagnetic fields as well as for characterizing internal degrees of freedom in the proximity of the NV.

In fact, this is what we want to discuss next. In Figure 3a (bottom) one notices additional features compared to the ideal TLS scenario which can only be explained through an extended treatment of the driven NV center that includes its close environment, shown in Fig. 3a (top). Namely, when the NV spin is operated around the GSLAC, the neighboring ^{15}N nuclear spin not only causes a hyperfine splitting but also hybridizes with the electronic spin states. Furthermore, within the GSLAC region, the optical initialization procedure is known to promote polarization transfer, resulting in an efficient population of the state $|m_S = 0, m_I = 1/2\rangle$ [25]. Thus, the TLS that is being driven with level spacing Δ_0 turns out to consist of this state and the hybridized state $|+\rangle_\alpha \equiv \alpha |-1, 1/2\rangle + \sqrt{1 - |\alpha|^2} |0, -1/2\rangle$, cf. [21]. However, other detuned transitions with comparable level spacings may also be driven for strong driving amplitudes. Aberrations between theory and experiment can be attributed to PL signal contributions from these transitions due to imperfect initialization and decay due to longitudinal relaxation. Such a detailed analysis, paired up with targeted experiments, is beyond the scope of this Letter but opens up avenues to quantitatively extract the initial state population distribution, the branching ratio $|\alpha|^2$, and thus precise values for hyperfine coupling constants as an alternative to the existing ODMR and EPR spectra.

Is it possible to reveal in the response of the driven TLS also period k -tupling with $k > 2$? In our experimental situation, this is indeed the case for $k = 3, 4$, and 5 as explicitly demonstrated in Fig. 3c and discussed in [21]. Although, the results were obtained with a coarser amplitude scan, the knowledge of the modulation period dependence on amplitude deviations from the ideal period k -tupling amplitude, still allows us to identify A_{Pk} with good precision. For all these cases, the hyperbola were found to fit $\tau \sim C_k/|A - A_{Pk}|$, wherein the coefficients C_k decrease with increasing k in agreement with theory.

Outlook. – An individual spin-1/2 realized in form of an NV-center in a diamond crystal has been shown to exhibit period doubling and higher multiplicities when exposed to strong time-period external fields. Within Floquet theory we have provided a complete and quantitatively accurate understanding of this non-trivial quantum dynamics in an extended

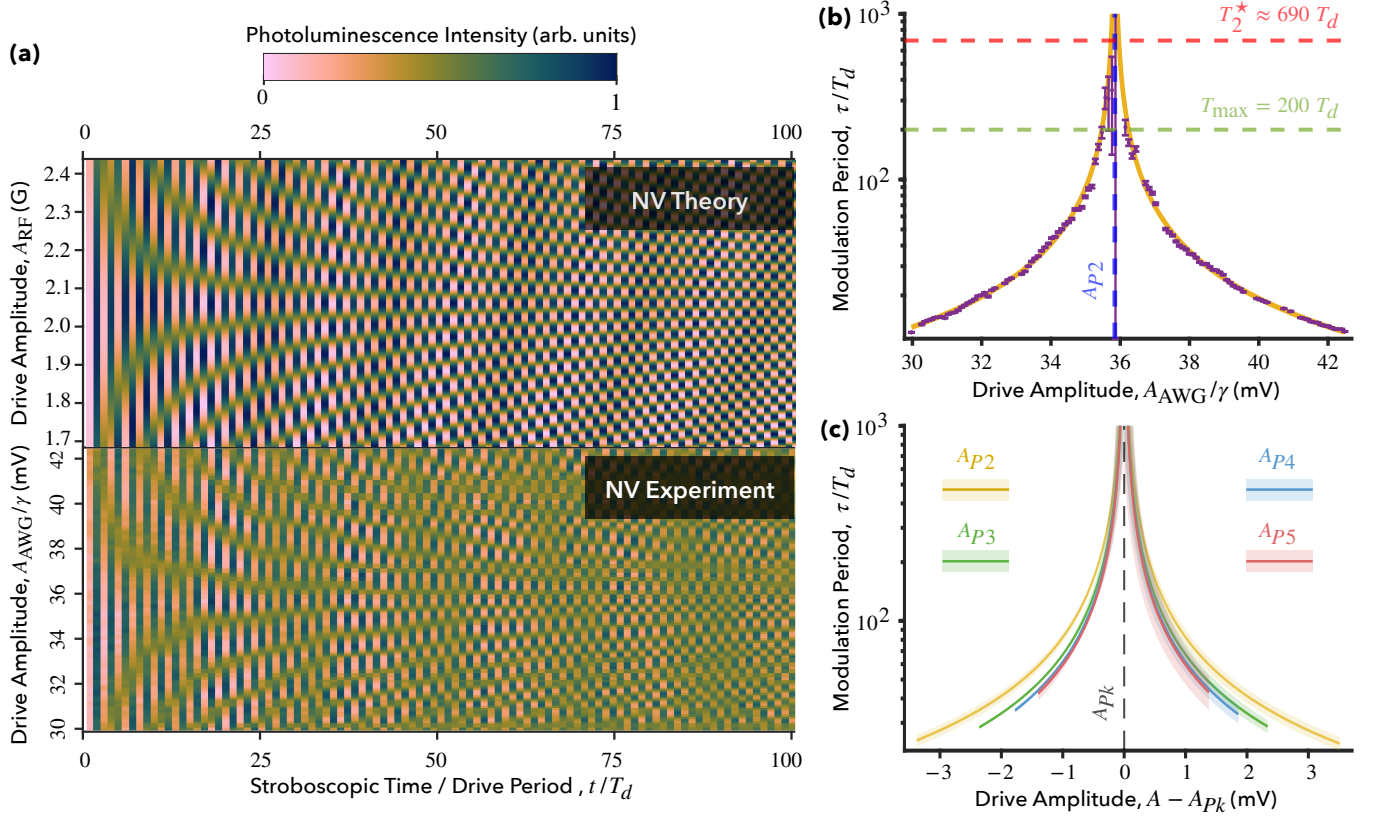


FIG. 3. (a) Experimental data for photoluminescence (PL) and extended theoretical modeling for period doubling. The PL signal recorded after every drive cycle (bottom) is compared to that estimated through simulation (top). The theoretical simulations are obtained within an extended model for driving the transition $\Delta_0 = 7.50$ MHz from $|0, 1/2\rangle$ to $|+\rangle_\alpha \equiv \alpha|-1, 1/2\rangle + (1 - |\alpha|^2)^{1/2}|0, -1/2\rangle$ for $|\alpha|^2 = 0.9044$ ($D_{\text{ZFS}} = 2.87$ GHz and $B_z = 1020.874$ G). The mean level spacing for the experimental setup is $\langle \Delta_0 \rangle = 9.21(5)$ MHz. In contrast to the pure TLS-treatment (Fig. 1), the extended model includes a nuclear spin of ^{15}N coupled to the electronic orbitals of the NV center. Minor residual differences between theory and experiment are due to the imperfect initialization and decay due to longitudinal relaxation. (b) The modulation period for period doubling fits the hyperbolic curve predicted by the extended model; hyperbola $A > A_{P2}$: $(79.731 \pm 0.433)/|A - A_{P2}|$, hyperbola $A < A_{P2}$: $(75.447 \pm 0.424)/|A - A_{P2}|$ so that the amplitude for period doubling is extracted as $A_{P2}(\text{exp}) = 35.844 \pm 0.018$ mV. (c) Same as (b) including higher multiplicities $k = 2, 3, 4, 5$ (for $\langle \Delta_0 \rangle = 7.88(20)$ MHz). See text and [21] for details.

model including relevant nuclear spins in the proximity of the NV-spin. In fact, in the vicinity of the ideal drive parameters for k -tupling, the NV-spin turns into a very sensitive probe for additional electromagnetic fields and residual degrees of freedom in its surrounding. This is the key property that may lead to new sensing scenarios. Further, the non-trivial k -tupling dynamics suggests the possibility of engineering gate operations with pulse times up to a few multiples of the transition frequency. Further extensions of this study may include the case of multiple dipolar coupled NV centers surrounded by ^{13}C instead of a single NV center [26] as well as the effect of magnetic field misalignment and unpolarized nuclear spins. Conceptually, our findings directly apply to any other realization in atomic and solid state physics with sufficient coherence times.

Acknowledgments– DD, RS, RSS, FJ and JA thank for financial support through the Baden-Württemberg Stiftung (QTBW-CDINQUA), RSS and FJ through the DFG, BMBF (Co-GeQ, SPINNING, QRX), QC-4-BW, and the ERC Synergy Grant

HyperQ, FJ and JA through the IQST, and JA through the BMBF (QSolid, QMAT within QSENS).

Author Contributions– DD developed the theoretical framework, proposed the experimental scheme, and analyzed the experimental data. RBG and RS performed the experiments together. JA and RSS coordinated the research collaboration. FJ and JA secured funding and provided overall supervision. JA, DD, RSS, RBG, and RS contributed to manuscript writing. All authors participated in reviewing and editing the final version.

Data Availability– Data available upon request.

* Corresponding Author: dhruv.deshmukh@uni-ulm.de; These authors contributed equally.

† These authors contributed equally.

[1] G. D. Fuchs, V. V. Dobrovitski, D. M. Toyli, F. J. Heremans, and D. D. Awschalom, Gigahertz dynamics of a strongly driven single quantum spin, *Science* **326**, 1520 (2009).

- [2] M. Wubs, Instantaneous coherent destruction of tunneling and fast quantum state preparation for strongly pulsed spin qubits in diamond, *Chemical Physics* **375**, 163 (2010).
- [3] X. Xu, B. Sun, E. D. Kim, K. Smirl, P. R. Berman, D. G. Steel, A. S. Bracker, D. Gammon, and L. J. Sham, Single charged quantum dot in a strong optical field: Absorption, gain, and the ac-stark effect, *Phys. Rev. Lett.* **101**, 227401 (2008).
- [4] Y. Sun, Y. Xu, and Z. Wang, The multi-rf photon transition driven by strong rf field in optical magnetic resonance of atoms, *Optics & Laser Technology* **145**, 107488 (2022).
- [5] G. C. Menard, A. Peugeot, C. Padurariu, C. Rolland, B. Kubala, Y. Mukharsky, Z. Iftikhar, C. Altimiras, P. Roche, H. le Sueur, P. Joyez, D. Vion, D. Esteve, J. Ankerhold, and F. Portier, Emission of photon multiplets by a dc-biased superconducting circuit, *Phys. Rev. X* **12**, 021006 (2020).
- [6] F. Grossmann, T. Dittrich, P. Jung, and P. Hänggi, Coherent destruction of tunneling, *Phys. Rev. Lett.* **67**, 516 (1991).
- [7] K. Sacha and J. Zakrzewski, Time crystals: a review, *Rep. Prog. Phys.* **81**, 016401 (2018).
- [8] L. Guo, *Phase Space Crystals* (IOP ebooks, 2021).
- [9] I.-M. Svensson, A. Bengtsson, P. Krantz, J. Bylander, V. Shumeiko, and P. Delsing, Period-tripling subharmonic oscillations in a driven superconducting resonator, *Phys. Rev. B* **96**, 174503 (2017).
- [10] L. Xiang, W. Jiang, Z. Bao, Z. Song, S. Xu, K. Wang, J. Chen, F. Jin, X. Zhu, Z. Zhu, *et al.*, Long-lived topological time-crystalline order on a quantum processor, *Nature Communications* **15**, 8963 (2024).
- [11] J. Zhang, P. W. Hess, A. Kyprianidis, P. Becker, A. Lee, J. Smith, G. Pagano, I.-D. Potirniche, A. C. Potter, A. Vishwanath, N. Y. Yao, and C. Monroe, Observation of a discrete time-crystal, *Nature* **543**, 217 (2017).
- [12] J. Smits, L. Liao, H. T. C. Stoof, and P. van der Straten, Observation of a space-time crystal in a superfluid quantum gas, *Phys. Rev. Lett.* **121**, 185301 (2018).
- [13] S. Choi, J. Choi, R. Landig, G. Kucsko, H. Zhou, J. Isoya, F. Jelezko, S. Onoda, H. Sumiya, V. Khemani, C. von Keyserlingk, N. Y. Yao, E. Demler, and M. D. Lukin, Observation of discrete time-crystalline order in a disordered dipolar many-body system, *Nature* **543**, 221 (2017).
- [14] S. Kohler, J. Lehmann, and P. Hänggi, Driven quantum transport on the nanoscale, *Phys. Rep.* **406**, 379 (2005).
- [15] M. I. Dykman, Coherent multiple-period states of periodically modulated qubits, *Phys. Rev. A* **100**, 042101 (2019).
- [16] F. Jelezko and J. Wrachtrup, Single defect centres in diamond: A review, *physica status solidi (a)* **203**, 3207 (2006).
- [17] J. M. Taylor, P. Cappellaro, L. Childress, L. Jiang, D. Budker, P. R. Hemmer, A. Yacoby, R. Walsworth, and M. D. Lukin, High-sensitivity diamond magnetometer with nanoscale resolution, *Nature Physics* **4**, 810 (2008).
- [18] F. Dolde, H. Fedder, M. W. Doherty, T. Nöbauer, F. Rempp, G. Balasubramanian, T. Wolf, F. Reinhard, L. C. Hollenberg, F. Jelezko, *et al.*, Electric-field sensing using single diamond spins, *Nature Physics* **7**, 459 (2011).
- [19] M. Grifoni and P. Hänggi, Driven quantum tunneling, *Physics Reports* **304**, 229 (1998).
- [20] V. Gramich, S. Gasparinetti, P. Solinas, and J. Ankerhold, Lamb-shift enhancement and detection in strongly driven superconducting circuits, *Phys. Rev. Lett.* **113**, 027001 (2014).
- [21] See Supplementary Material.
- [22] J. P. Tetienne, L. Rondin, P. Spinicelli, M. Chipaux, T. Debuisschert, J.-F. Roch, and V. Jacques, Magnetic-field-dependent photodynamics of single nv defects in diamond: an application to qualitative all-optical magnetic imaging, *New Journal of Physics* **14**, 103033 (2012).
- [23] V. Jacques, P. Neumann, J. Beck, M. Markham, D. Twitchen, J. Meijer, F. Kaiser, G. Balasubramanian, F. Jelezko, and J. Wrachtrup, Dynamic polarization of single nuclear spins by optical pumping of nitrogen-vacancy? format? color centers in diamond at room temperature, *Physical review letters* **102**, 057403 (2009).
- [24] J. M. Binder, A. Stark, N. Tomek, J. Scheuer, F. Frank, K. D. Jahnke, C. Müller, S. Schmitt, M. H. Metsch, T. Uden, *et al.*, Qudi: A modular python suite for experiment control and data processing, *SoftwareX* **6**, 85 (2017).
- [25] D. A. Broadway, J. D. A. Wood, L. T. Hall, A. Stacey, M. Markham, D. A. Simpson, J.-P. Tetienne, and L. C. L. Hollenberg, Anticrossing spin dynamics of diamond nitrogen-vacancy centers and all-optical low-frequency magnetometry, *Phys. Rev. Appl.* **6**, 064001 (2016).
- [26] L. J. I. Moon, P. M. Schindler, R. J. Smith, E. Druga, Z.-R. Zhang, M. Bukov, and A. Ajoy, Discrete time crystal sensing, *arXiv preprint arXiv:2410.05625* (2024).
- [27] S. Felton, A. M. Edmonds, M. E. Newton, P. M. Martineau, D. Fisher, D. J. Twitchen, and J. M. Baker, Hyperfine interaction in the ground state of the negatively charged nitrogen vacancy center in diamond, *Phys. Rev. B* **79**, 075203 (2009).
- [28] C. A. Coulson and M. J. Kearsley, Colour centres in irradiated diamonds. I, *Proc. R. Soc. Lond. A* **241**, 433 (1957).

Supplementary Material for

Observation of period doubling and higher multiplicities in a driven single-spin system

CONTENTS

References	4
SI.I: On Period k -tupling in NV Center	SI.2
A. Applicability of TLS theory	SI.2
B. Period k -tupling: A first look	SI.3
C. Period-doubling and neighborhood	SI.5
D. Period-tripling and neighborhood	SI.7
E. Period-quadrupling and neighborhood	SI.10
F. Period-quintupling and neighborhood	SI.14
G. Period k -tupling: Summary of Results	SI.19
SI.II: On Details of Period Doubling Results	SI.20
A. Theoretical Modeling of a driven NV center	SI.20
B. Detailed comparison of theoretical and experimental results	SI.22
C. Extraction of the dominant PL signal	SI.23
SI.III: Experimental Details	SI.26
A. Sample preparation	SI.26
B. Experimental setup	SI.26
C. Experimental procedure	SI.26

SI.I: ON PERIOD k -TUPLING IN NV CENTER

A. Applicability of TLS theory

The k -tupling phenomena, which has been theoretically predicted for a linearly driven TLS, is being tested here through the photoluminescence (PL) signal emitted from a driven ^{15}N NV center. Instead of the simple Hamiltonian for a linearly driven TLS, we now have the Hamiltonian [27],

$$\begin{aligned} H(t) = & D_{\text{ZFS}}(S_z^2 - 2/3) - \gamma_{\text{NV},z} S_z B_z - \gamma_{\text{nuc}} I_z B_z \\ & + A_{\parallel} S_z I_z + A_{\perp} (S_x I_x + S_y I_y) \\ & - \gamma_{\text{NV},x} S_x A_{\text{RF}} \sin(\omega_d t) - \gamma_{\text{nuc}} I_x A_{\text{RF}} \sin(\omega_d t). \end{aligned}$$

The observable (PL signal) depends solely on the electronic state population distribution. The applicability of the TLS theory in predicting k -tupling phenomena in an NV center, and its observation via the PL signal, therefore becomes nuanced and one has to carefully consider the following points:

- The TLS (selected by tuning B_z to operate the system near GSLAC) comprises of the state $|0, 1/2\rangle$ (electronic spin projection $m_S = 0$, nuclear spin projection $m_I = 1/2$). and the state $|\alpha\rangle$ which is a hybridized spin state.
- These states are driven predominantly through the S_x operator that drives the electronic spin states. The effect of driving nuclear spin through I_x can be safely neglected due to weak nuclear gyromagnetic ratio.
- The state initialization to $|0, 1/2\rangle$ is known to be efficient [25] but still not perfect.
- For strong driving amplitudes A_{RF} , the effect of the neighboring ^{15}N nuclear spin upon the electronic spin dynamics via the hyperfine coupling cannot be neglected.
- In addition, one also observes decay in the PL signal due to environmental interactions.

In the remainder of **SI.I**, we show the PL signal results for a coarse-grained amplitude scan obtained for an effective TLS with a low apparent hybridization. We find a good agreement between the NV center results with those expected from TLS theory, especially for lower drive amplitudes. Additional faint features in the PL signal, due to the coupled ^{15}N nuclear spin, reveal themselves only for higher driving amplitudes (around the period-doubling amplitude). In **SI.II**, we separately discuss the period-doubling case in greater detail, wherein we address these extra features.

B. Period k -tupling: A first look

Stroboscopically recorded PL signal along with its discrete Fourier transform (DFT) is shown in Fig. SI.1. The characteristic alternating pattern of period-doubling signal along with its modulation for the neighboring amplitudes can be clearly seen in the PL signal heatmap. For higher k , it becomes increasingly harder to visually find and confirm period k -tupling through the heatmap. This is due to the following reasons:

1. A multi-color pattern needs to be tracked, and a visual confirmation of the revival of this pattern with some tolerance is challenging.
2. Even at the amplitude closest to the k -tupling amplitude, in the coarse-grained amplitude scan, there may be a slow, yet noticeable, modulation of the pattern.
3. The experimental data will also show longitudinal relaxation to a mixed-state for longer drive durations. This limits the number of repetitions of the pattern, that can be faithfully confirmed.

The knowledge of k -tupling phenomena along with its modulation in the neighborhood of k -tupling manifold, from the TLS theory, helps us unravel the PL signal data of the driven NV dynamics. Thus, we can quantitatively confirm the presence of k -tupling dynamics in NV center despite the relaxation in the dynamics due to environmental interactions, and the presence of additional frequency components due to the interaction with neighboring nuclear spin.

To this end, we first decompose the PL signal into k sequences for each amplitude in the neighborhood of the period k -tupling amplitude, A_{Pk} . These sequences, labeled by $l \in \{1, \dots, k\}$, are PL signals recorded after the pulse time $t_m = (m \cdot k + l)T_d$, where $m \in \mathbb{Z}$. Thus, they represent PL signals recorded every k periods starting from the initial state $|\psi(l \cdot T_d)\rangle$. Note that all of these sequences are related across the full range of amplitudes as the primary initial state is still $|\psi(t=0)\rangle \approx |0, 1/2\rangle$.

Such a deconstruction allows us to treat all k -tupling cases on equal footing. If the amplitude of the drive was aligned perfectly to A_{Pk} , we would ideally expect (as per closed system dynamics) all the sequences to be constants equal to the PL intensities corresponding to the states $|\psi(l \cdot T_d)\rangle$. Slight deviation in amplitude to $\tilde{A} = A_{Pk} + \delta A$ would induce an oscillation in these PL sequences with the same modulation period. Following the TLS theory, we expect the modulation period, τ , to show a hyperbolic dependence upon the qED deviation from k -tupling condition: $\tau = |1/\xi|$, where $\Delta\varepsilon/\hbar\omega_d = (j/k + \xi) \bmod 1$. For moderate drive amplitudes ($A < \Delta_0$) and in-tune driving ($\omega_d = \Delta_0$), this translates to an approximate hyperbolic dependence on the amplitude deviation δA from A_{Pk} : $\tau \approx |1/\delta A|$. The next four subsections show experimental data corroborating this behavior for $k = 2, 3, 4$, and 5 , along with the ineludible environmental decay and weak signals from the nuclear spin as discussed above.

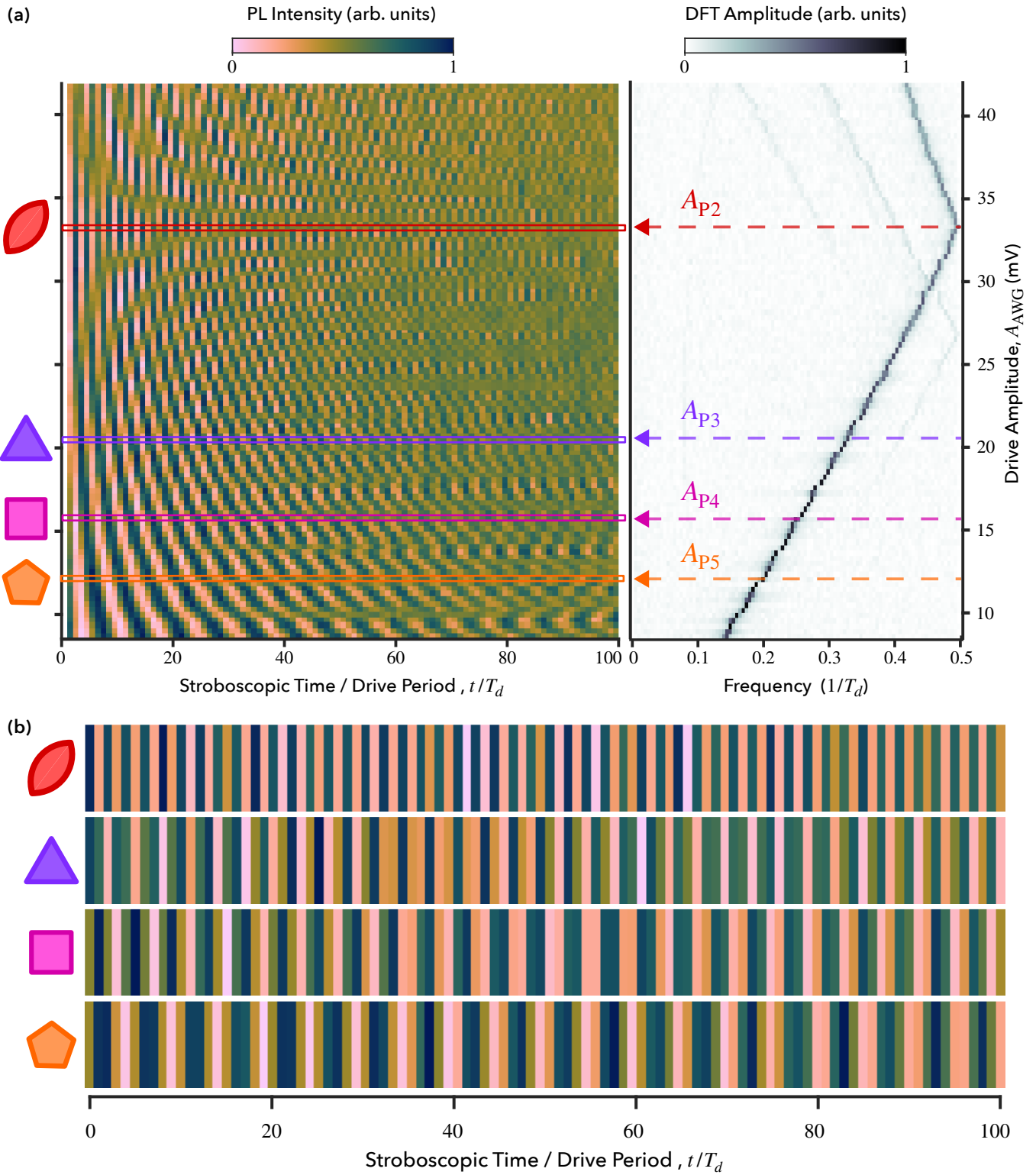


FIG. SI.1. (a) The left panel shows PL signal intensity captured stroboscopically after driving the NV center for integer number of periods. The panel on the right contains the DFT of this signal (captured for $200 T_d$). The period k -tupling amplitudes, A_{Pk} , are marked for $k = 2, 3, 4,$ and 5 . The DFT shows that for weaker amplitudes there is only one main frequency contribution to PL signal, and contributions from driving other detuned transitions become noticeable only for stronger amplitudes. Figure (b) shows stroboscopically recorded PL intensity patterns for sampling amplitudes that are closest to A_{Pk} for $k = 2, 3, 4,$ and 5 .

C. Period-doubling and neighborhood

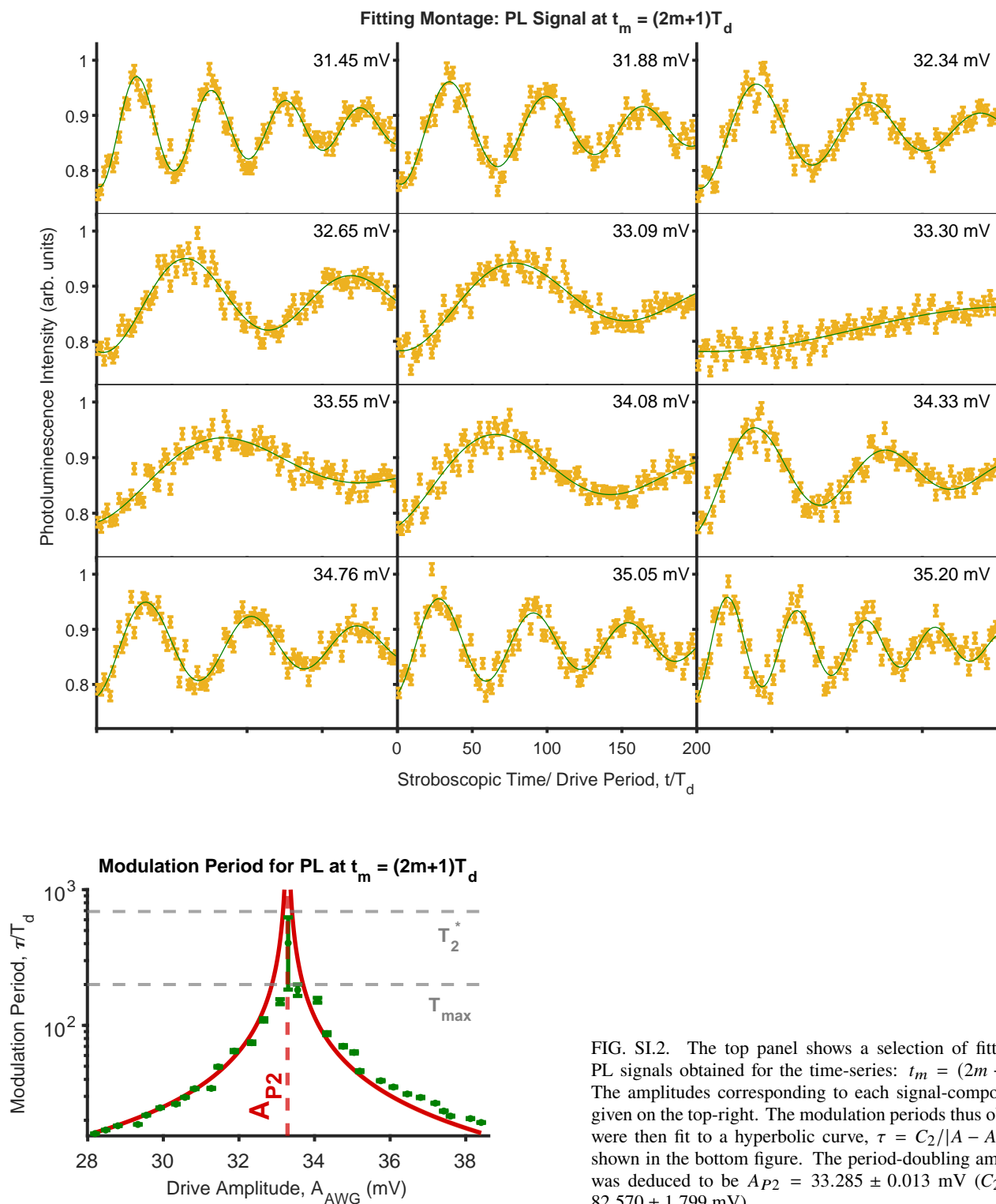


FIG. SI.2. The top panel shows a selection of fittings to PL signals obtained for the time-series: $t_m = (2m + 1)T_d$. The amplitudes corresponding to each signal-component is given on the top-right. The modulation periods thus obtained were then fit to a hyperbolic curve, $\tau = C_2/|A - A_{P2}|$, as shown in the bottom figure. The period-doubling amplitude was deduced to be $A_{P2} = 33.285 \pm 0.013$ mV ($C_2/T_d = 82.570 \pm 1.799$ mV).

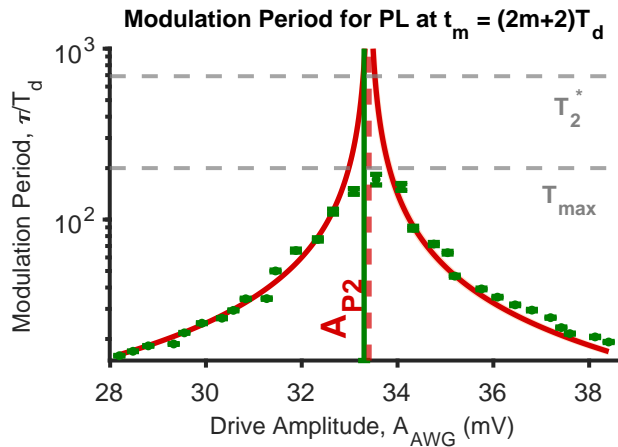
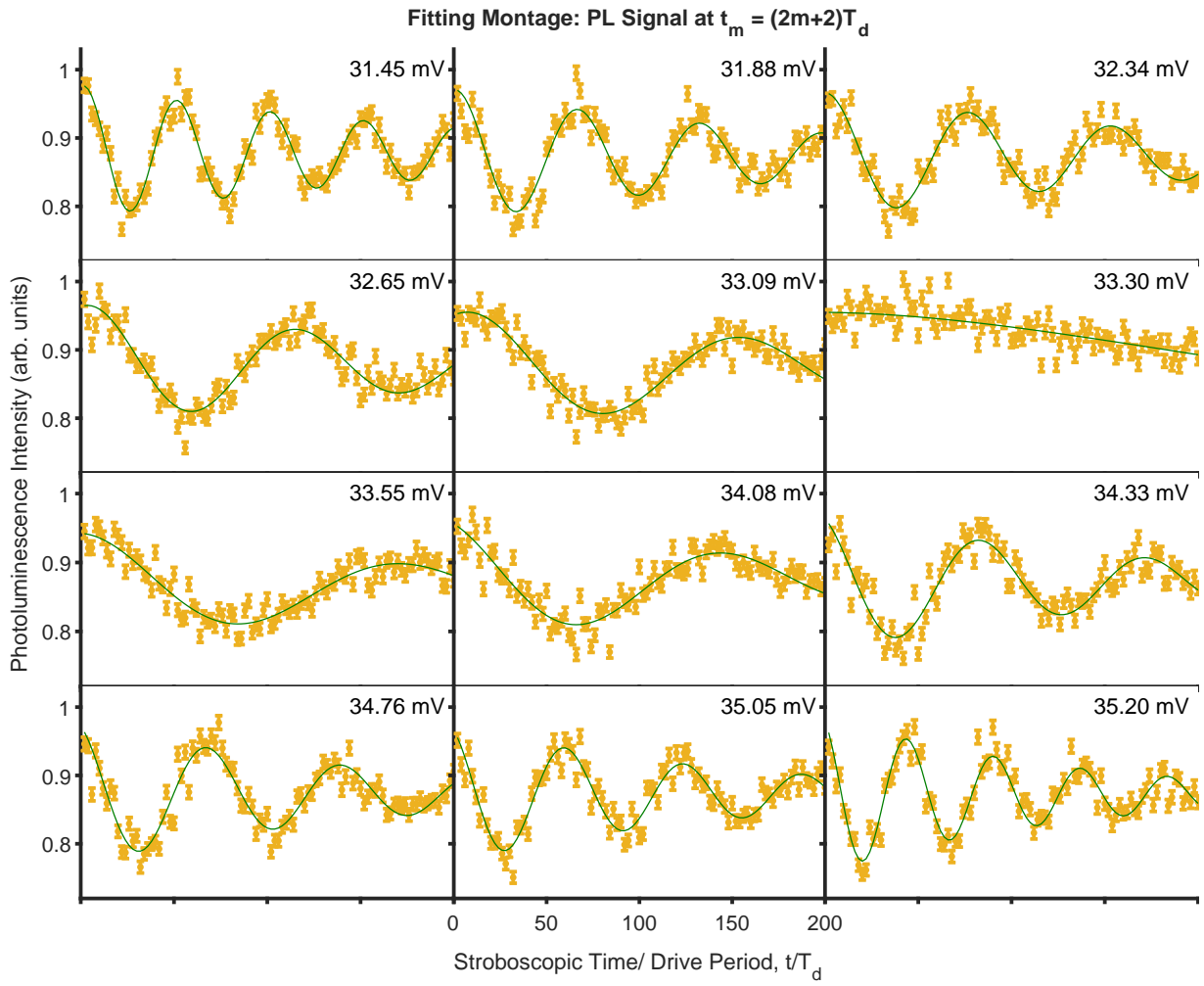


FIG. SI.3. The top panel shows a selection of fittings to PL signals obtained for the time-series: $t_m = (2m + 2)T_d$. The amplitudes corresponding to each signal-component is given on the top-right. The modulation periods thus obtained were then fit to a hyperbolic curve, $\tau = C_2/|A - A_{P2}|$, as shown in the bottom figure. The period-doubling amplitude was deduced to be $A_{P2} = 33.405 \pm 0.034$ mV ($C_2/T_d = 84.388 \pm 1.513$ mV).

D. Period-tripling and neighborhood

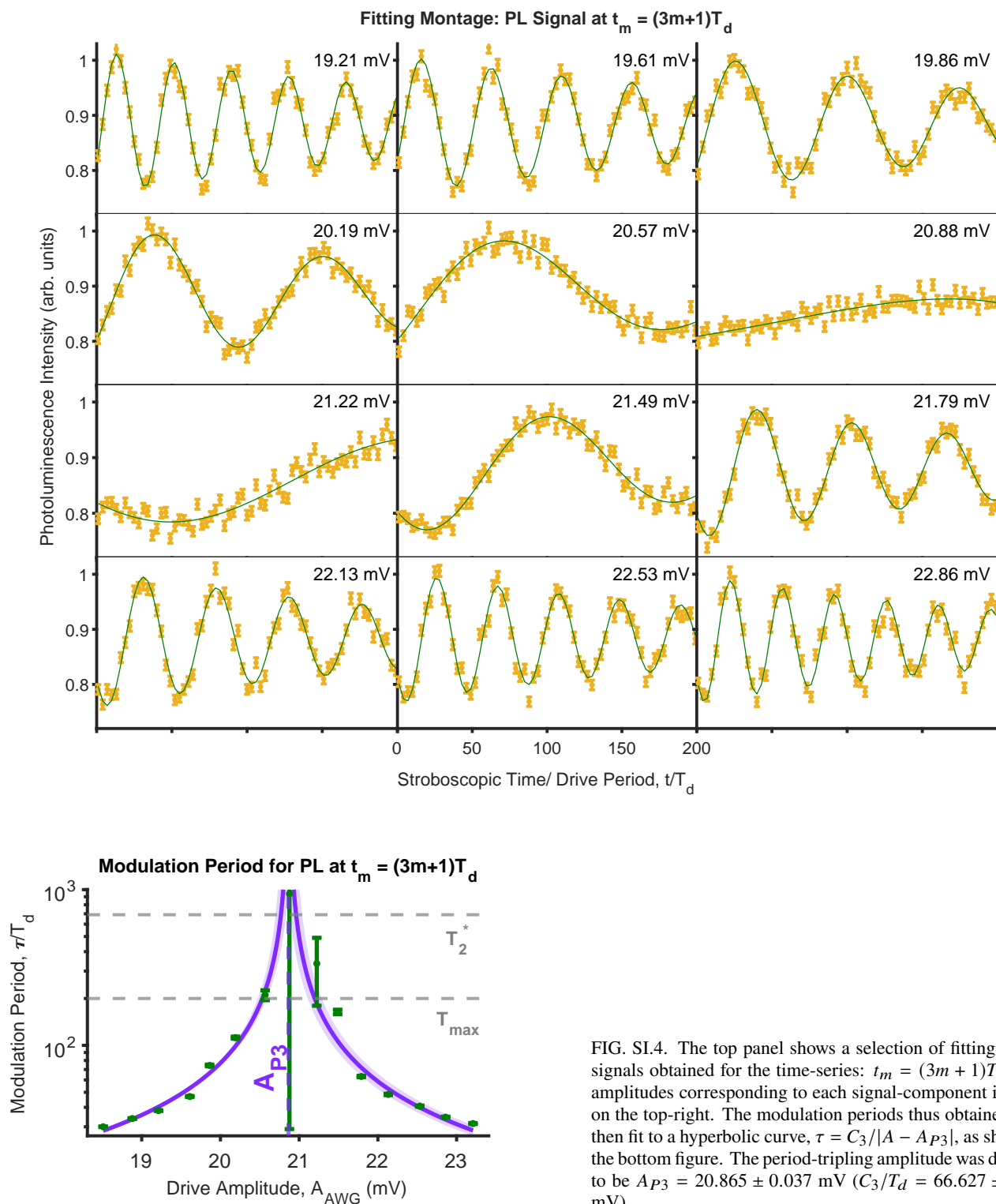


FIG. SI.4. The top panel shows a selection of fittings to PL signals obtained for the time-series: $t_m = (3m + 1)T_d$. The amplitudes corresponding to each signal-component is given on the top-right. The modulation periods thus obtained were then fit to a hyperbolic curve, $\tau = C_3/|A - A_{P3}|$, as shown in the bottom figure. The period-tripling amplitude was deduced to be $A_{P3} = 20.865 \pm 0.037$ mV ($C_3/T_d = 66.627 \pm 1.636$ mV).

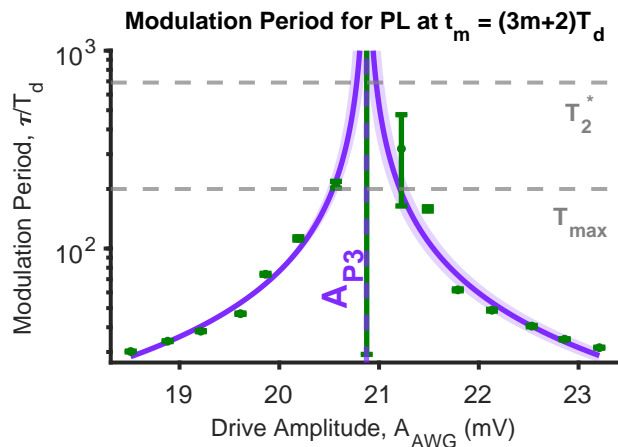
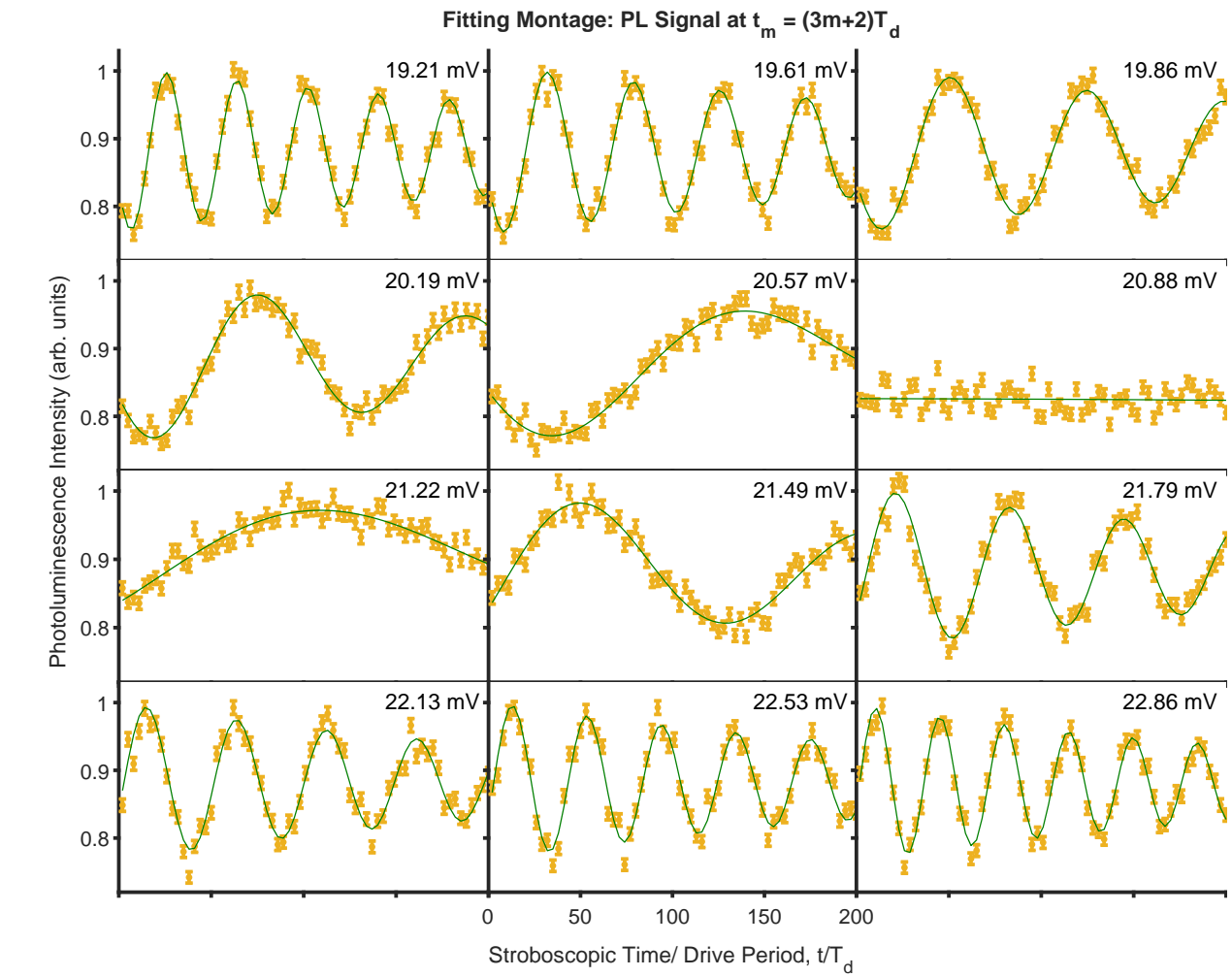


FIG. SI.5. The top panel shows a selection of fittings to PL signals obtained for the time-series: $t_m = (3m + 2)T_d$. The amplitudes corresponding to each signal-component is given on the top-right. The modulation periods thus obtained were then fit to a hyperbolic curve, $\tau = C_3/|A - A_{P3}|$, as shown in the bottom figure. The period-tripling amplitude was deduced to be $A_{P3} = 20.874 \pm 0.038$ mV ($C_3/T_d = 67.133 \pm 1.653$ mV).

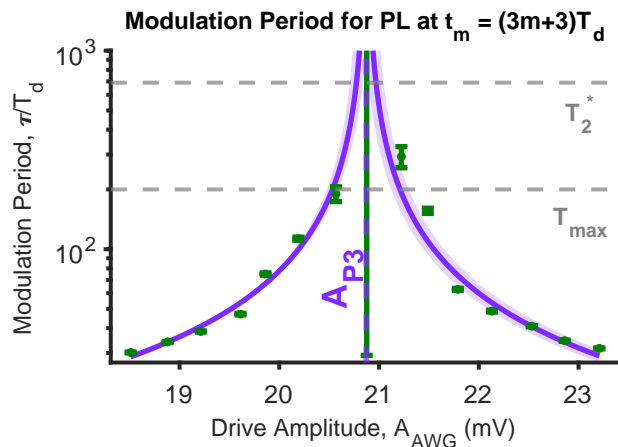
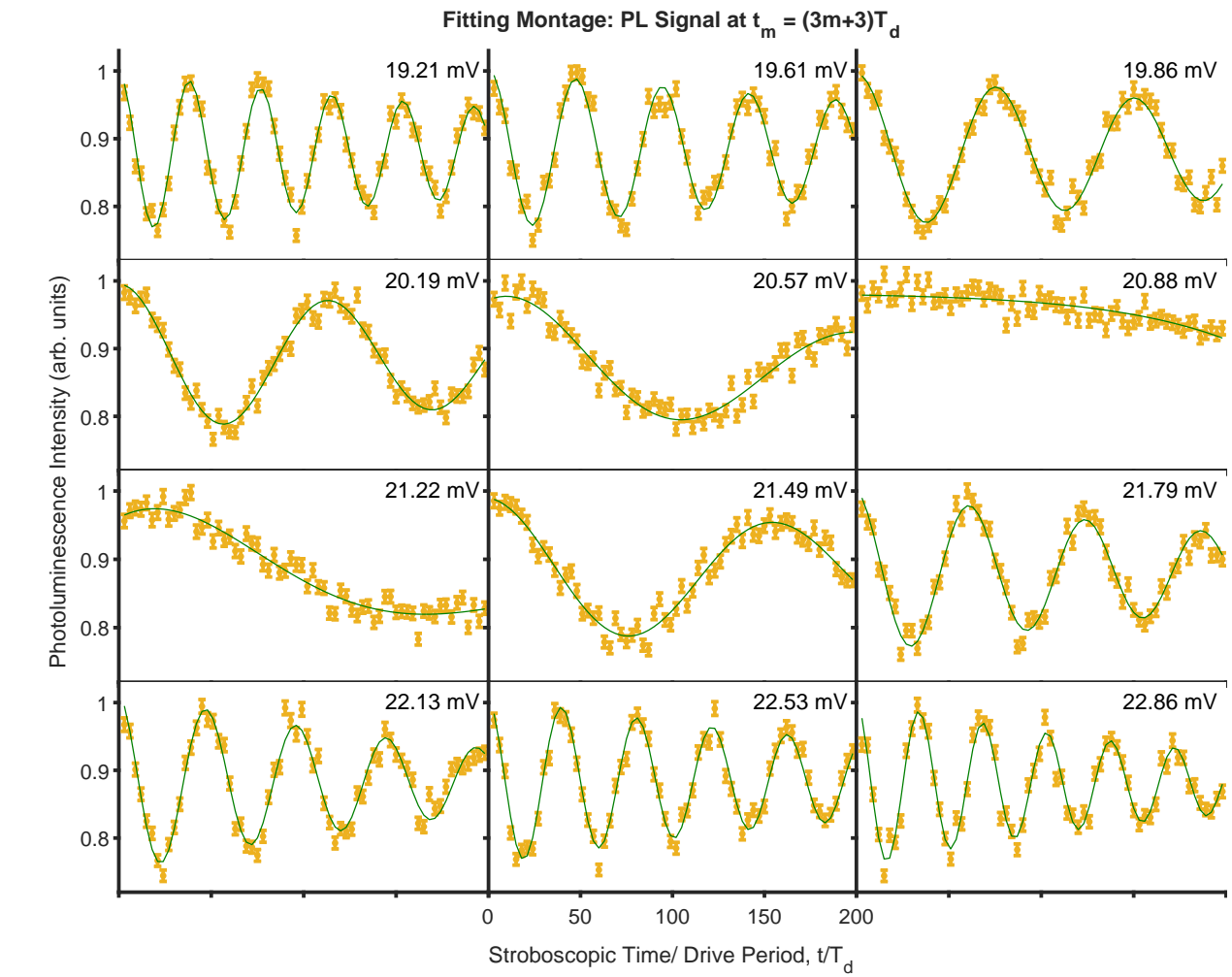


FIG. SI.6. The top panel shows a selection of fittings to PL signals obtained for the time-series: $t_m = (3m + 3)T_d$. The amplitudes corresponding to each signal-component is given on the top-right. The modulation periods thus obtained were then fit to a hyperbolic curve, $\tau = C_3/|A - A_{P3}|$, as shown in the bottom figure. The period-tripling amplitude was deduced to be $A_{P3} = 20.871 \pm 0.037$ mV ($C_3/T_d = 67.758 \pm 1.568$ mV).

E. Period-quadrupling and neighborhood

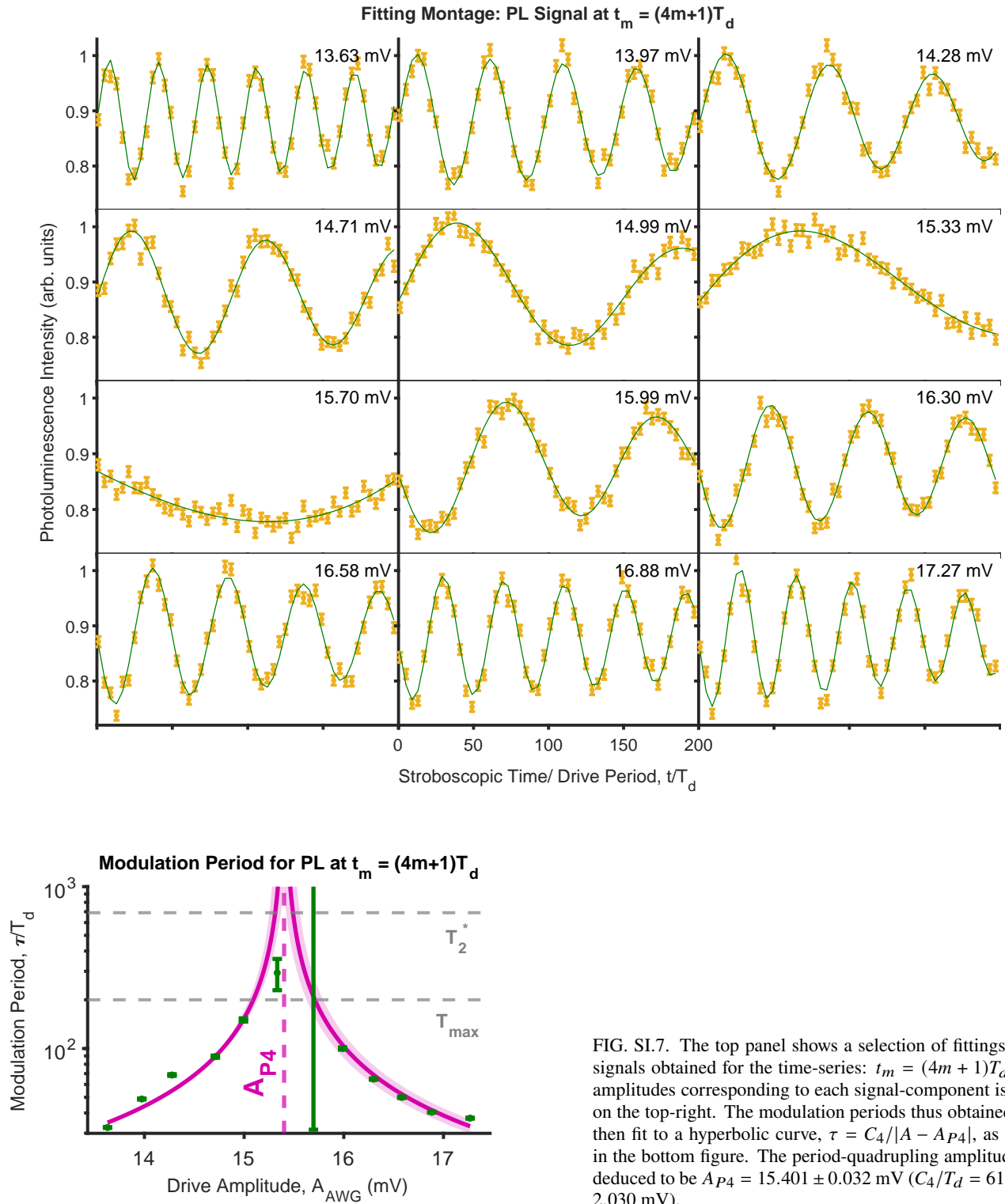


FIG. SI.7. The top panel shows a selection of fittings to PL signals obtained for the time-series: $t_m = (4m + 1)T_d$. The amplitudes corresponding to each signal-component is given on the top-right. The modulation periods thus obtained were then fit to a hyperbolic curve, $\tau = C_4/|A - A_{P4}|$, as shown in the bottom figure. The period-quadrupling amplitude was deduced to be $A_{P4} = 15.401 \pm 0.032$ mV ($C_4/T_d = 61.737 \pm 2.030$ mV).

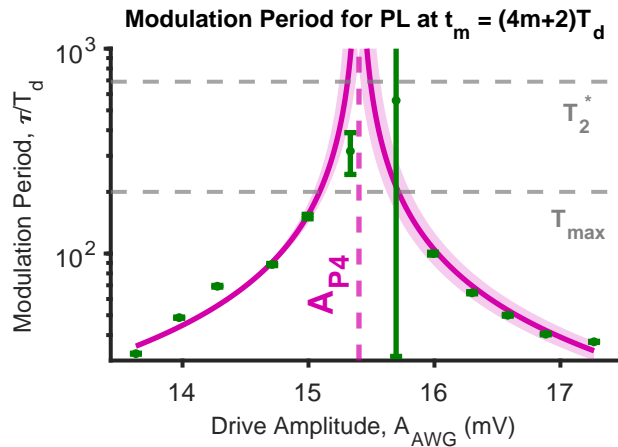
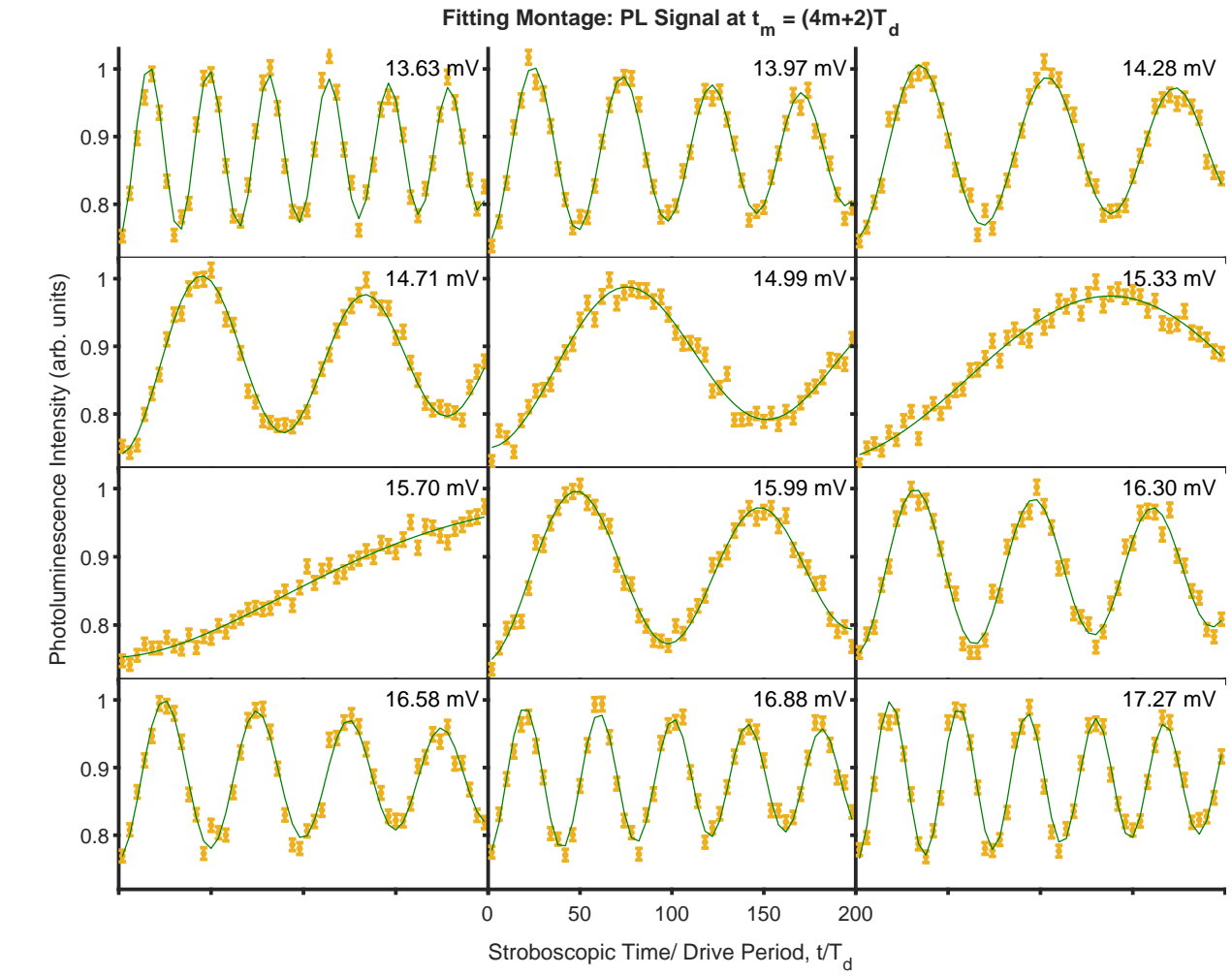


FIG. SI.8. The top panel shows a selection of fittings to PL signals obtained for the time-series: $t_m = (4m + 2)T_d$. The amplitudes corresponding to each signal-component is given on the top-right. The modulation periods thus obtained were then fit to a hyperbolic curve, $\tau = C_4/|A - A_{P4}|$, as shown in the bottom figure. The period-quadrupling amplitude was deduced to be $A_{P4} = 15.401 \pm 0.037$ mV ($C_4/T_d = 62.548 \pm 2.191$ mV).

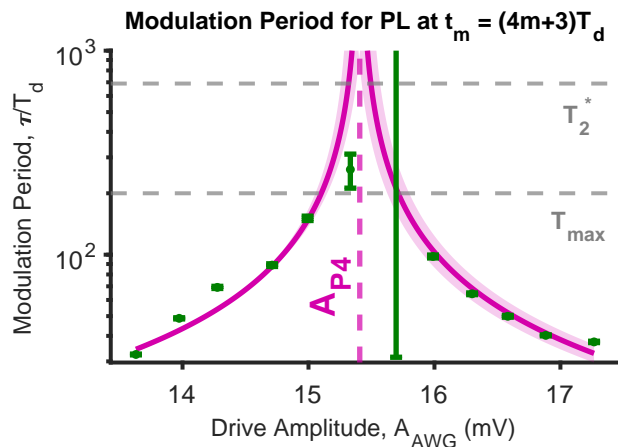
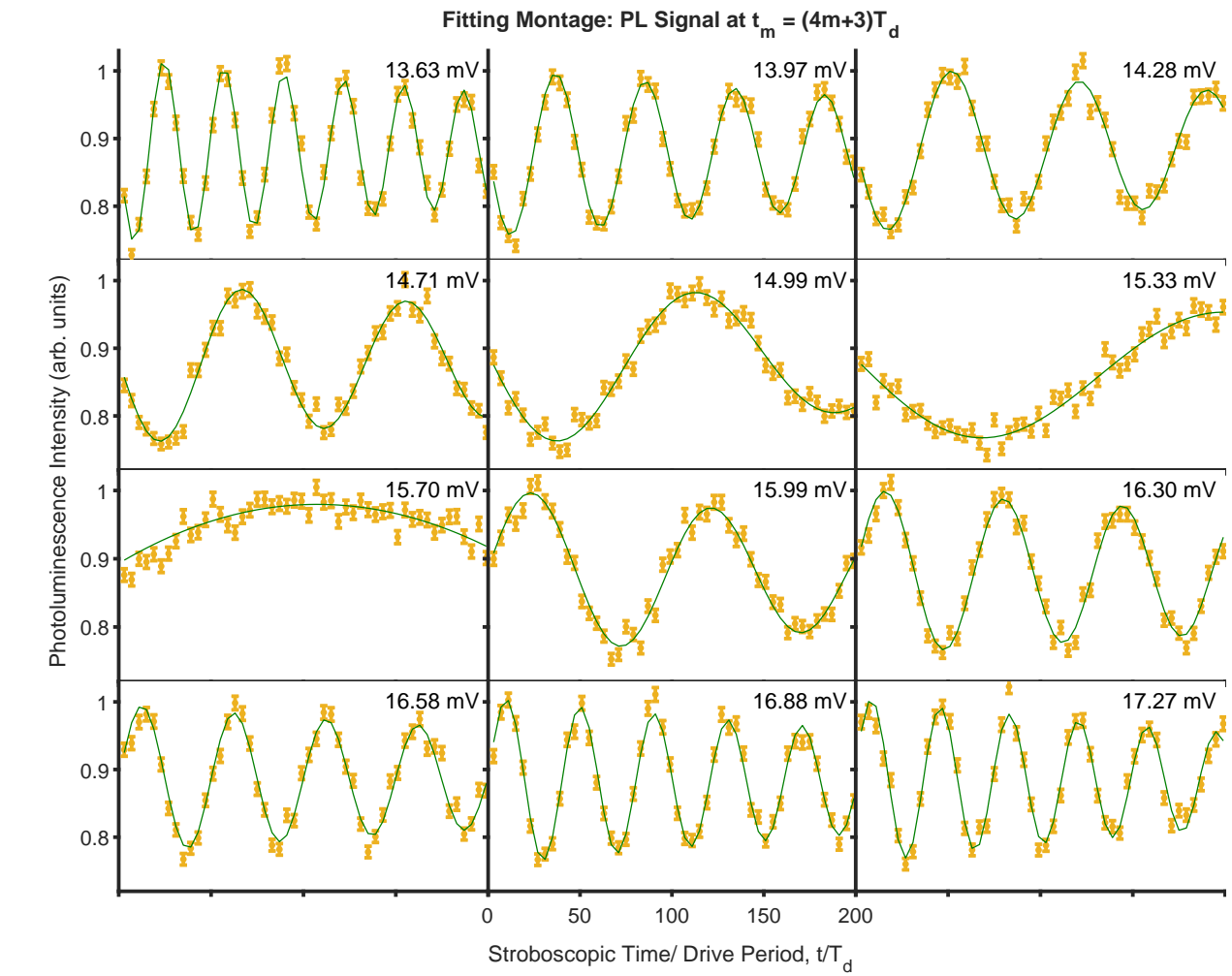


FIG. SI.9. The top panel shows a selection of fittings to PL signals obtained for the time-series: $t_m = (4m + 3)T_d$. The amplitudes corresponding to each signal-component is given on the top-right. The modulation periods thus obtained were then fit to a hyperbolic curve, $\tau = C_4/|A - A_{P4}|$, as shown in the bottom figure. The period-quadrupling amplitude was deduced to be $A_{P4} = 15.407 \pm 0.034$ mV ($C_4/T_d = 61.090 \pm 2.052$ mV).

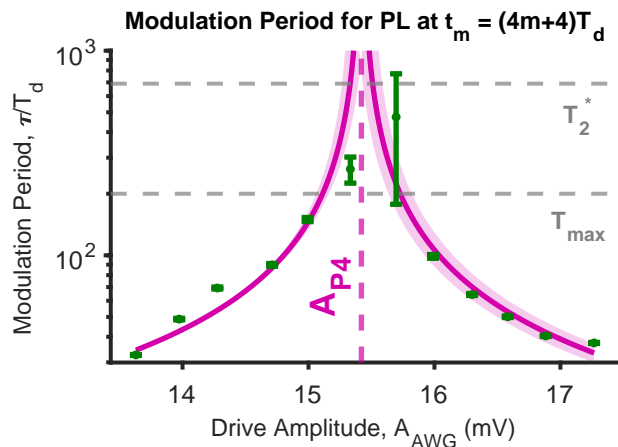
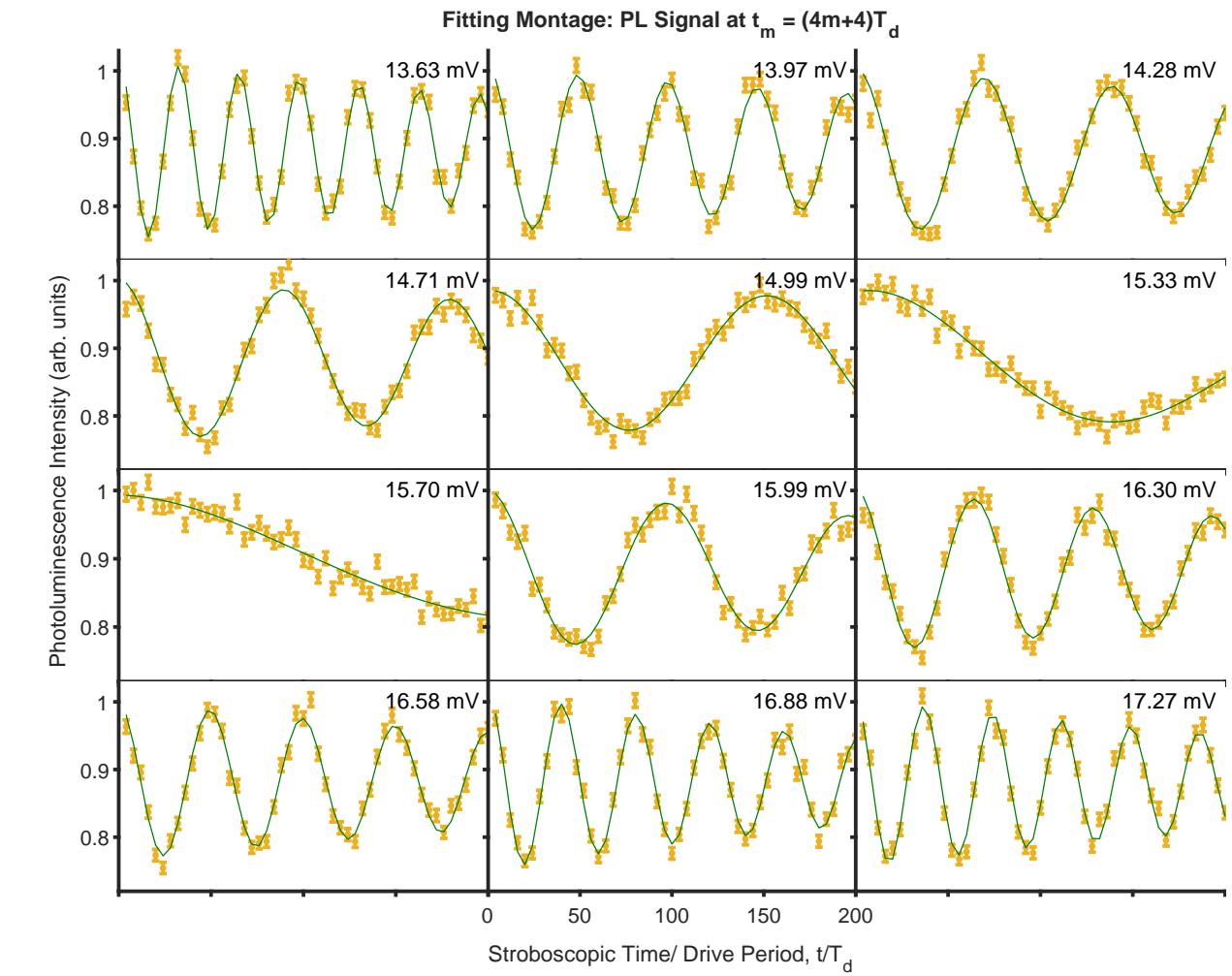


FIG. SI.10. The top panel shows a selection of fittings to PL signals obtained for the time-series: $t_m = (4m + 4)T_d$. The amplitudes corresponding to each signal-component is given on the top-right. The modulation periods thus obtained were then fit to a hyperbolic curve, $\tau = C_4/|A - A_{P4}|$, as shown in the bottom figure. The period-quadrupling amplitude was deduced to be $A_{P4} = 15.420 \pm 0.036$ mV ($C_4/T_d = 61.616 \pm 2.130$ mV).

F. Period-quintupling and neighborhood

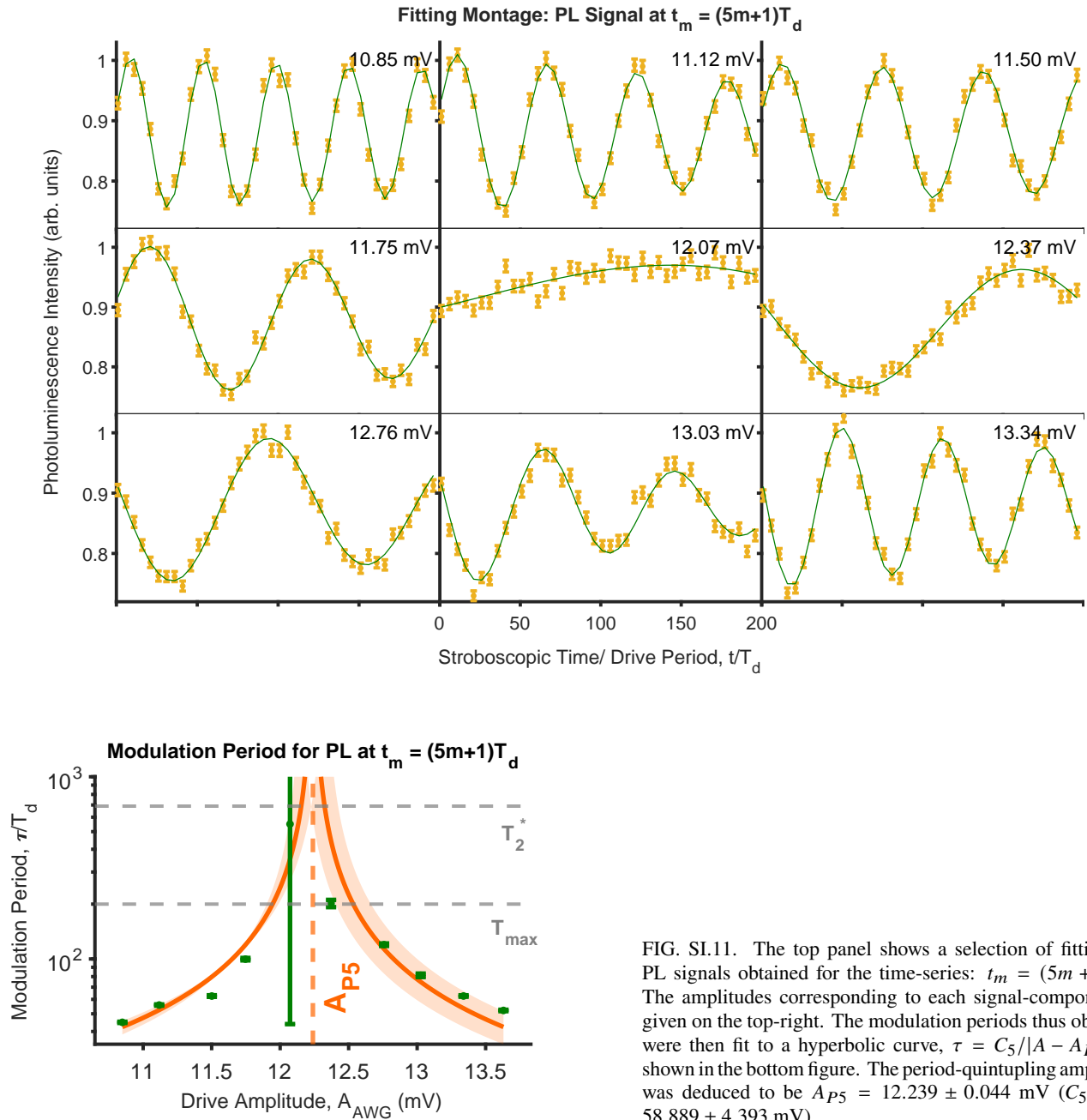


FIG. SI.11. The top panel shows a selection of fittings to PL signals obtained for the time-series: $t_m = (5m + 1)T_d$. The amplitudes corresponding to each signal-component is given on the top-right. The modulation periods thus obtained were then fit to a hyperbolic curve, $\tau = C_5/|A - A_{P5}|$, as shown in the bottom figure. The period-quintupling amplitude was deduced to be $A_{P5} = 12.239 \pm 0.044$ mV ($C_5/T_d = 58.889 \pm 4.393$ mV).

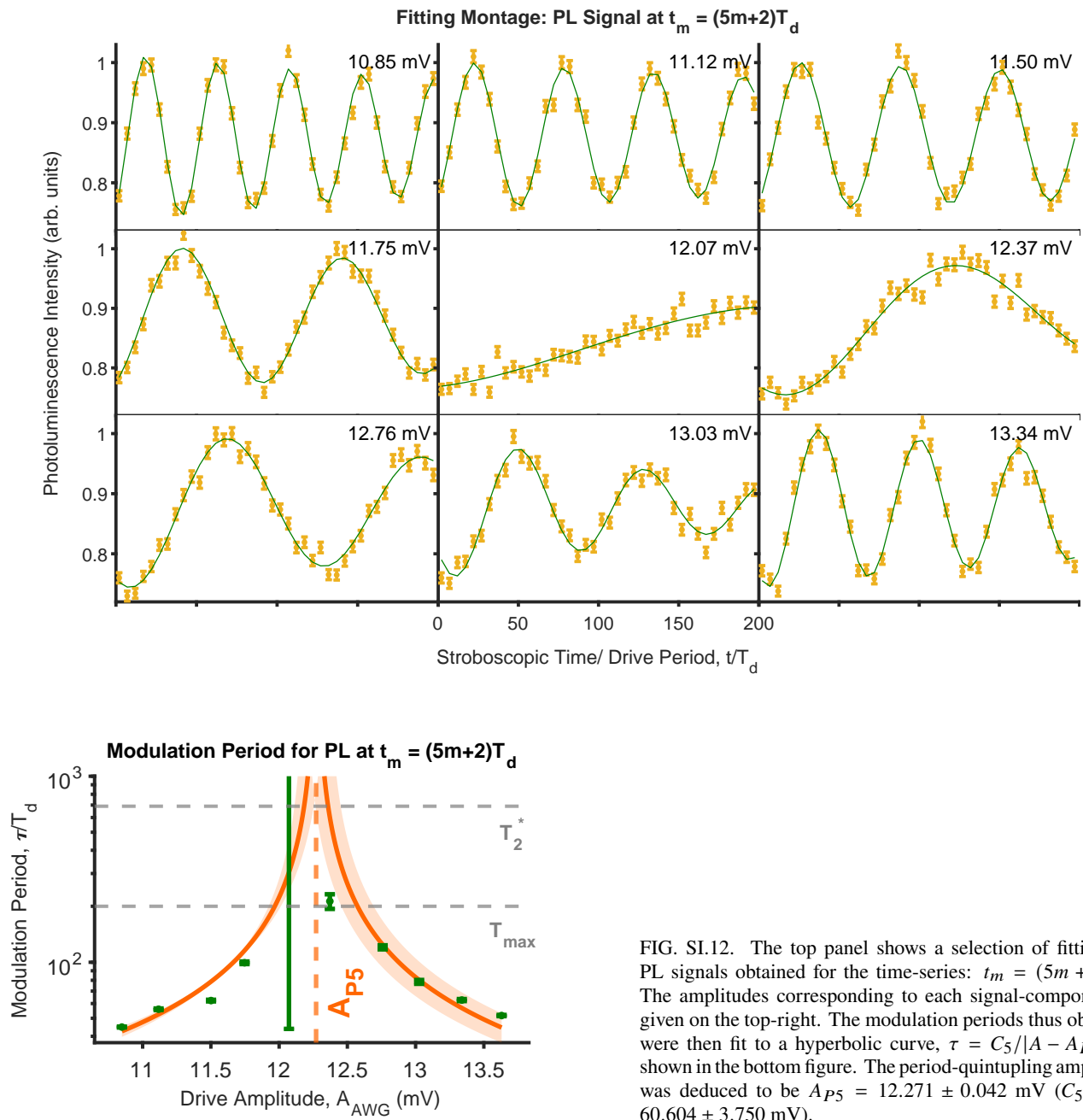


FIG. SI.12. The top panel shows a selection of fittings to PL signals obtained for the time-series: $t_m = (5m + 2)T_d$. The amplitudes corresponding to each signal-component is given on the top-right. The modulation periods thus obtained were then fit to a hyperbolic curve, $\tau = C_5/|A - A_{P5}|$, as shown in the bottom figure. The period-quintupling amplitude was deduced to be $A_{P5} = 12.271 \pm 0.042$ mV ($C_5/T_d = 60.604 \pm 3.750$ mV).

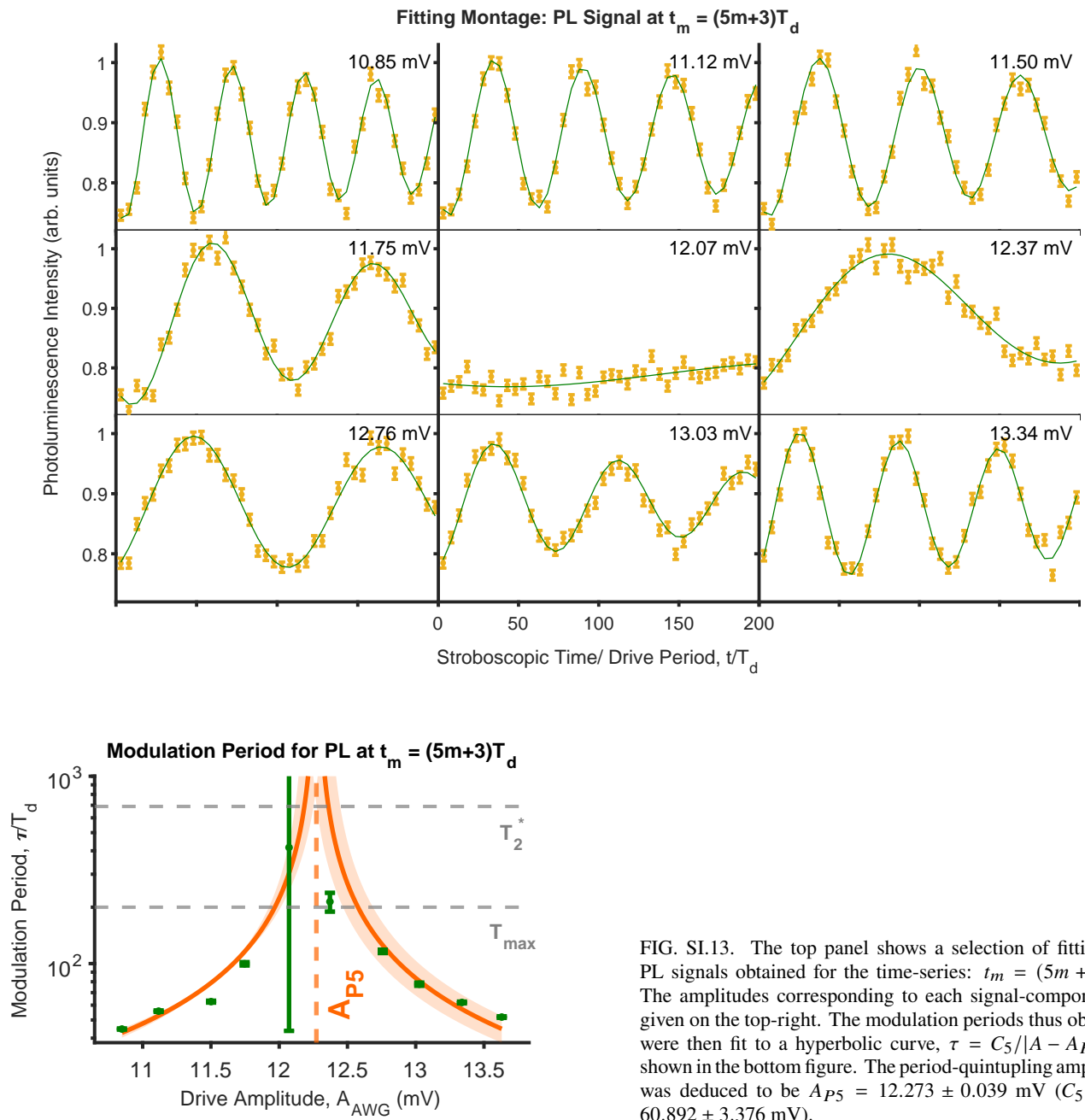


FIG. SI.13. The top panel shows a selection of fittings to PL signals obtained for the time-series: $t_m = (5m + 3)T_d$. The amplitudes corresponding to each signal-component is given on the top-right. The modulation periods thus obtained were then fit to a hyperbolic curve, $\tau = C_5/|A - A_{P5}|$, as shown in the bottom figure. The period-quintupling amplitude was deduced to be $A_{P5} = 12.273 \pm 0.039$ mV ($C_5/T_d = 60.892 \pm 3.376$ mV).

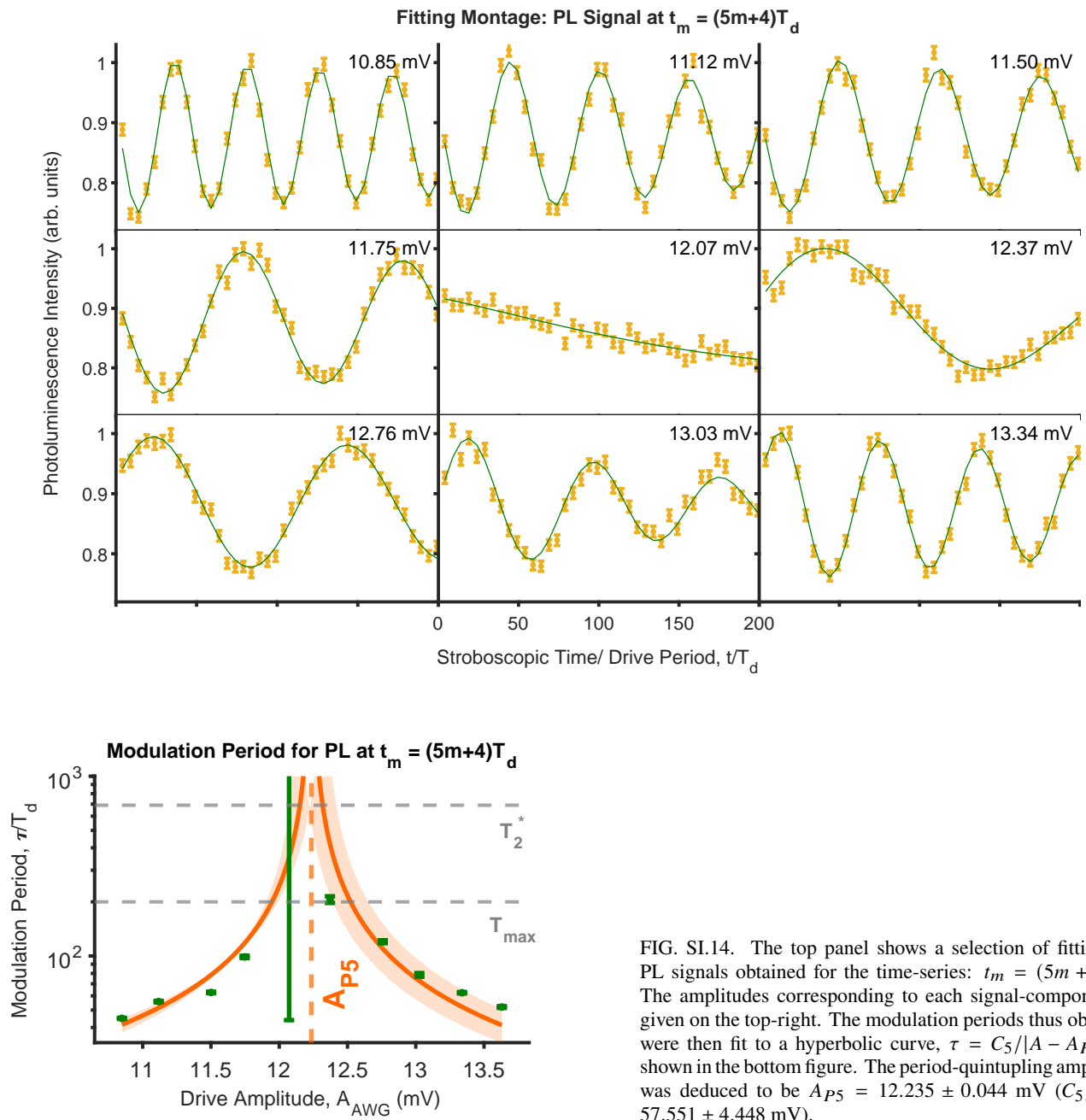


FIG. SI.14. The top panel shows a selection of fittings to PL signals obtained for the time-series: $t_m = (5m + 4)T_d$. The amplitudes corresponding to each signal-component is given on the top-right. The modulation periods thus obtained were then fit to a hyperbolic curve, $\tau = C_5/|A - A_{P5}|$, as shown in the bottom figure. The period-quintupling amplitude was deduced to be $A_{P5} = 12.235 \pm 0.044$ mV ($C_5/T_d = 57.551 \pm 4.448$ mV).

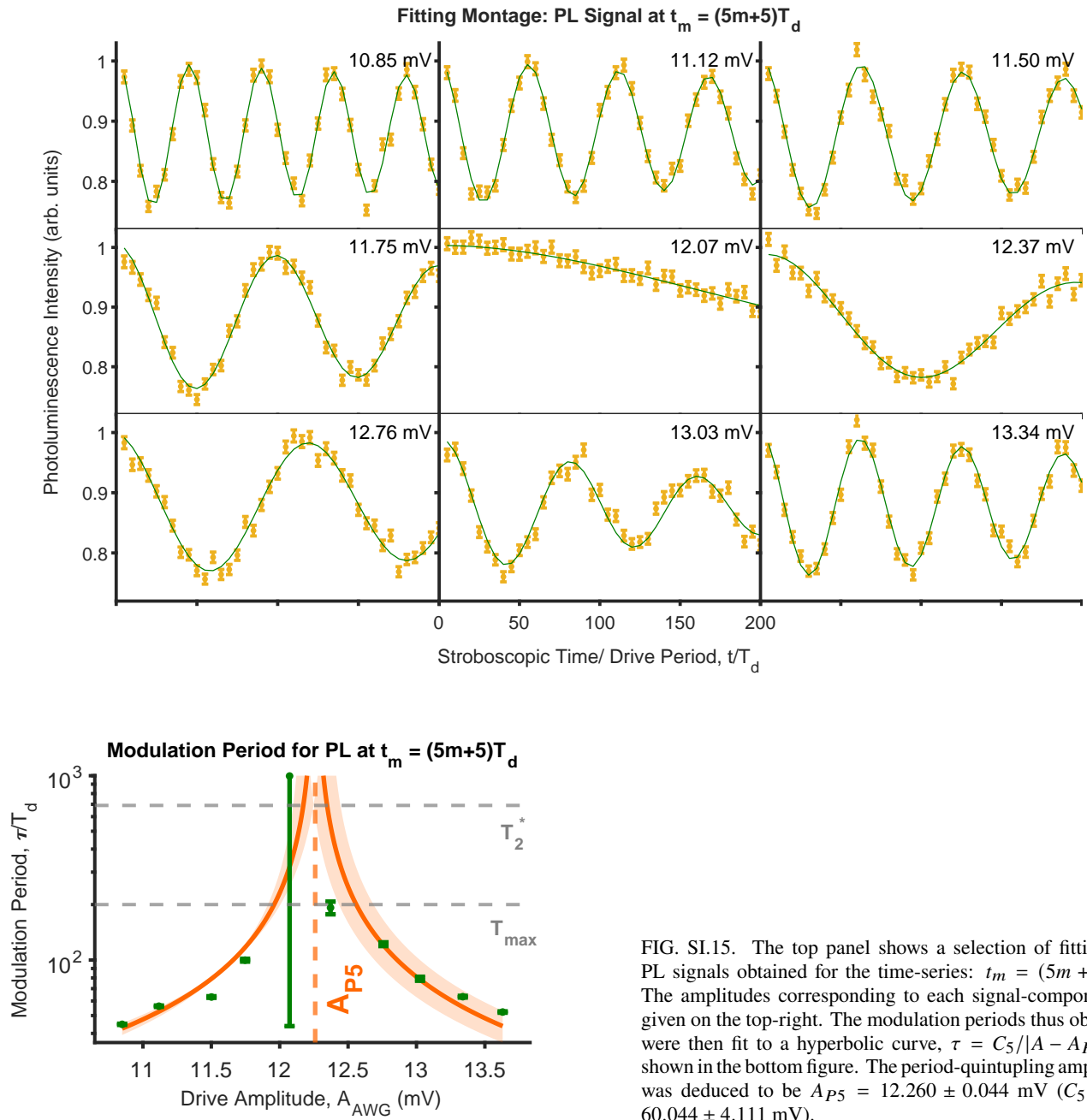


FIG. SI.15. The top panel shows a selection of fittings to PL signals obtained for the time-series: $t_m = (5m + 5)T_d$. The amplitudes corresponding to each signal-component is given on the top-right. The modulation periods thus obtained were then fit to a hyperbolic curve, $\tau = C_5/|A - A_{P5}|$, as shown in the bottom figure. The period-quintupling amplitude was deduced to be $A_{P5} = 12.260 \pm 0.044$ mV ($C_5/T_d = 60.044 \pm 4.111$ mV).

G. Period k -tupling: Summary of Results

Given below are the results for averaged modulation time period fit. These values correspond to the curves plotted in **FIG. 3(c)**.

k	$A_{Pk}(mV)$	$C_k/T_d(mV)$
2	33.294 ± 0.010	82.429 ± 3.104
3	20.870 ± 0.036	67.167 ± 1.622
4	15.408 ± 0.035	61.740 ± 2.117
5	12.249 ± 0.043	59.371 ± 4.137

TABLE I. Values of A_{Pk} and C_k/T_d used in the modulation period fit for period k -tupling.

SI.II: ON DETAILS OF PERIOD DOUBLING RESULTS

A. Theoretical Modeling of a driven NV center

We now discuss the manner and extent to which the dynamics of a strongly driven NV center deviates from that of an ideal driven TLS. In the previous section, we have outlined factors that render this discussion nuanced; here, we address these complications in stages. We start by considering the simplest TLS realization using a single NV center. The experimental setup restricts the maximum achievable drive amplitude which is required to implement in the experimental protocol in the strong driving regime. This forces us to tune the background magnetic field to approach the GSLAC, in order to obtain a TLS with low level-spacing. A detailed analysis of the driven NV center near the GSLAC, assessing the validity of the TLS approximation, is presented below.

- **TLS from electronic-spin eigenstates:**

The system of choice for this experiment is a negatively charged $^{15}\text{NV}^-$ center. Specifically, we are interested in the lowest energy eigenstates of the molecular orbitals (defect-molecule approach [28]) formed by the two unpaired electrons within the Nitrogen-Vacancy complex. The ground state manifold, denoted by 3A_2 , has a spin-triplet configuration with total spin $S = 1$. Introducing a background magnetic field B_z , aligned with the NV axis, (Zeeman) splits the degenerate states $|m_S = \pm 1\rangle$. Thus, by tuning B_z , we can reduce the energy-level spacing between $|m_S = -1\rangle$ and $|m_S = 0\rangle$ to realize strong driving, whilst simultaneously pushing $|m_S = +1\rangle$ sufficiently high in energy to validate the truncation of the Hilbert space to the two-level system spanned by $|-1\rangle$ and $|0\rangle$, even under strong driving (see Fig. SI.16 (a)). This TLS can then be driven by a periodic magnetic field $A_x \sin \omega_d t$ which couples to the electronic spin states via the spin operator S_x . The observation of state populations is inferred through the (integrated) photoluminescence signal emitted after an optical excitation to the spin triplet manifold 3E is triggered. The states, $|0\rangle$ and $|\pm 1\rangle$, correspond to the brightest and darkest PL signal, respectively.

- **Electronic-spin TLS $\{|-1\rangle, |0\rangle\}$ and the ^{15}N nuclear spin:**

The hyperfine interaction between the chosen TLS, $\{|-1\rangle, |0\rangle\}$, and the ^{15}N nuclear spin, yields two manifolds of states, with $m_S = 0$ and $m_S = -1$, respectively. In the $|m_S, m_I\rangle$ spin-eigenstate basis, the four resulting energy eigenstates — listed in descending values of energy — are:

$$|-1, -1/2\rangle, |-1, 1/2\rangle, |0, 1/2\rangle, \text{ and } |0, -1/2\rangle.$$

The energy difference between the two transitions,

$$|0, -1/2\rangle \xleftrightarrow{\Delta_\downarrow} |-1, -1/2\rangle \text{ and } |0, 1/2\rangle \xleftrightarrow{\Delta_\uparrow} |-1, 1/2\rangle,$$

becomes resolvable when they are tuned down to ~ 100 MHz (see Fig. SI.16 (b)). Thus, for weak driving (Rabi regime), one may be able to resonantly drive just one of these transitions. However, in the strong driving regime, the detuned transition is also driven. Also, the initialization process through optical excitation is expected to produce a mixed initial state with equal probability of nuclear spin orientations in the $m_S = 0$ manifold. Thus, a minimal treatment of strongly driven NV center requires considering two non-interacting TLS with different level spacings. Consequently, the driven NV center effectively behaves as two electronic TLS sharing a common drive $\sim A_{\text{RF}} \sin(\omega_d t) S_x$, and the PL signal reports the electronic spin projection distribution between the $m_S = 0$ and $m_S = -1$ manifolds, with contributions from both TLS.

- **TLS from energy eigenstates near GSLAC:** As we reduce the level-spacing further, we enter the region of ground-state level anti-crossing (GSLAC). The spin-eigenstates are no longer the energy-eigenstates. The states $|-1, 1/2\rangle$ and $|0, -1/2\rangle$ hybridize due to the presence of the non-secular transverse component of the hyperfine coupling. The new energy eigenstates are $|-1, -1/2\rangle$, $|0, 1/2\rangle$, $|+\rangle_\alpha$, and $|-\rangle_\alpha$ (see Fig. SI.16 (c)), where

$$\begin{aligned} |+\rangle_\alpha &\equiv \alpha |-1, 1/2\rangle + \sqrt{1 - |\alpha|^2} |0, -1/2\rangle, \text{ and} \\ |-\rangle_\alpha &\equiv \alpha |0, -1/2\rangle - \sqrt{1 - |\alpha|^2} |-1, 1/2\rangle. \end{aligned}$$

One benefit of operating the NV center in this regime is that the initialization process also does efficient polarization transfer, thus initializing the state in $|0, 1/2\rangle$ state. However, this regime also comes with its own complications. The TLS of choice comprises of the energy eigenstates $|0, 1/2\rangle$ and $|+\rangle_\alpha$ with level spacing Δ_0 . And, the driving term $-\gamma_{\text{NV},x} S_x A_{\text{RF}} \sin(\omega_d t)$ is not diagonal in the energy-eigenstates basis. Therefore, other detuned transitions will also be driven with the same drive. For a fair comparison with the ideal driven TLS theory, we use a renormalized amplitude given as:

$$\bar{A} = \langle \alpha; + | -\gamma_{\text{NV},x} S_x | 0, 1/2 \rangle A_{\text{RF}} / \Delta_0$$

Furthermore, the two extremes of PL signals are also not representative of the states of the chosen TLS. This reduces the contrast in comparison to the ideal driven TLS theory. Despite these complications, the dominant contribution in the PL signal can be extracted and ratifies the TLS treatment of the driven NV center. Caution must still be exercised here - if the system is tuned deeper into the GSLAC region with high hybridization, a full driven NV center theory becomes indispensable.

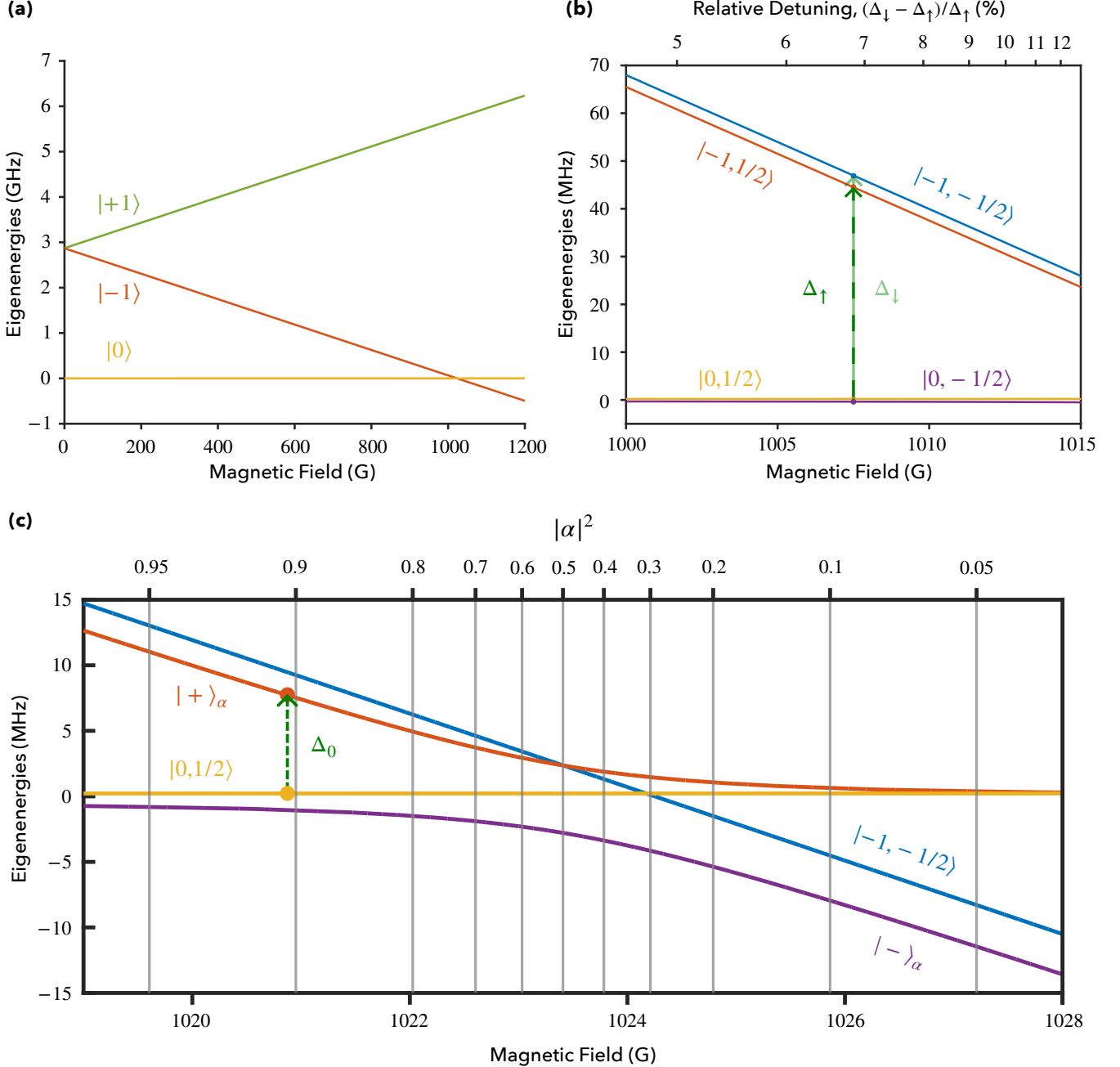


FIG. SI.16. Eigenenergies of a single ^{15}NV center as a function of background magnetic field ($D_{\text{ZFS}} = 2.87$ GHz). (a) shows the m_S levels $|1\rangle$, $|-1\rangle$, and $|0\rangle$. (b) shows the manifolds $m_S = -1$ and $m_S = 0$ with two hyperfine levels each. The energy difference between the transitions Δ_{\uparrow} and Δ_{\downarrow} becomes resolvable as shown via the relative detuning. (c) shows the energy eigenstates in the GSLAC region, along with their hybridization quantified by $|\alpha|^2$. The driven dynamics for the specific instance of TLS, marked by $\Delta_0 = 7.5$ MHz ($B_z = 1020.874$ G; $|\alpha|^2 = 0.9044$), is discussed next.

B. Detailed comparison of theoretical and experimental results

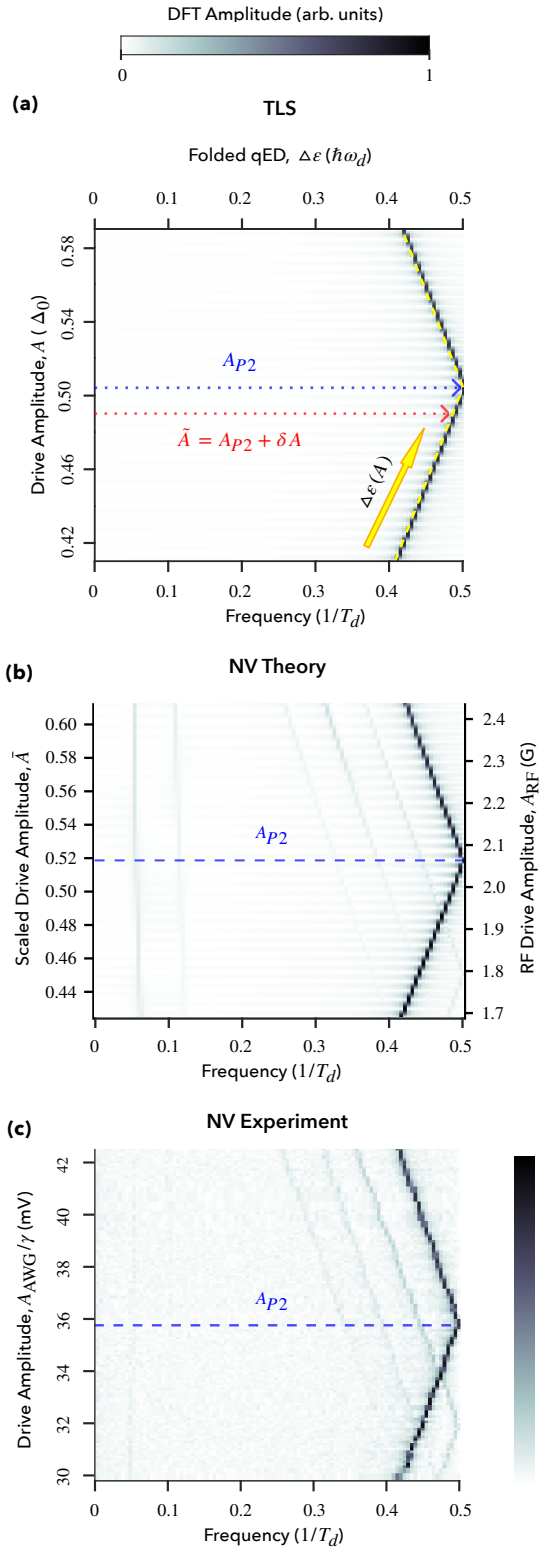


FIG. SI.17. Figure (a) shows the Discrete Fourier Transform (DFT) corresponding to the stroboscopic population projection for a driven TLS as shown in **FIG 1**. Figure (c) shows the DFT of the experimentally recorded PL signal as shown in **FIG 3(a) - bottom**, wherein the main transition of $\langle \Delta_0 \rangle \approx 9.21$ MHz was driven. Figure (b) represents the DFT of numerically computed PL intensities for a driven NV center with parameters tuned to match the DFT in (c). Here, the drive-frequency, ω_d , was chosen to be in tune with the level-spacing $\Delta_0 = 7.50$ MHz, as delineated in Fig. SI.16.

In the main article, we have showcased the stroboscopic observable measurements in the neighborhood of the period-doubling amplitude A_{P2} , for a driven TLS model (**FIG 1**), an NV model (**FIG 3(a)** - top), and the experiment (**FIG 3(a)** - bottom). Qualitative differences between these results were noted. We now give a brief exposition on the similarities and differences between these observations, with the aid of their DFTs (see Fig. **SI.17**).

The Discrete Fourier Transform (DFT) of TLS shows only one dominant frequency ridge (Fig. **SI.17** (a)). This ridge precisely lies on the quasi-energy difference (qED; folded back from 0.5). The experimental result on the other hand, shows multiple faint ridges in addition to the dominant ridge as predicted by the TLS theory (Fig. **SI.17** (c)). These extra frequency responses can be understood by an extensive model of driven NV near GSLAC, as discussed above. The DFT shown in Fig. **SI.17** (b), shows a pattern similar to that of the experimental results. The level-spacing for this case, $\Delta_0 = 7.5$ MHz, was set a little lower than the mean level spacing for experiments $\Delta_0 = 9.21(5)$ MHz. This was necessary to match the relative positions of the faint features in the DFT. The discrepancy is thought to be due to the drifts and fluctuation in the level-spacing during the experiment. These are caused by the relative motion between the magnet producing the bias field and the stage on which the diamond (NV center) is placed. Another culprit could be the drift in $D_{ZFS}(T)$, due to the Joule heating of the copper wire as a result of the high power RF generation for the long duration of the entire amplitude scanning protocol. Since the pulsed-ODMR was performed in a limited frequency range, level-spacing for other transitions were not available. This makes it difficult to precisely identify the complete eigenenergy configuration for the NV center. The simulations indicate that the hybridization of the NV center levels, in the experimental setup, should yield $|\alpha|^2 \approx 0.90$. Further careful experimentation including complete ODMR, amplitude and photoluminescence calibration, would help establish this quantitatively. In conclusion, we note that despite some faint features, the experimental results of the driven NV center predominantly show a response in accordance with that of driven TLS behavior.

C. Extraction of the dominant PL signal

Having noted the dominance of driven TLS character in the experimental results of a driven NV, we now explicitly show the fitting of this dominant response to the full PL signal in Fig. **SI.18** and Fig. **SI.19**. These fits show the expected modulating behavior as the drive amplitude departs from the period-doubling amplitude A_{P2} . The average modulation period for each amplitude was used to produce **FIG 3(b)** in the main article. The decay in the modulated envelope has been phenomenologically added in the model. The oscillations about the dominant signals capture the information about the initialization, energy level-structure, and the hybridization of the driven NV system.

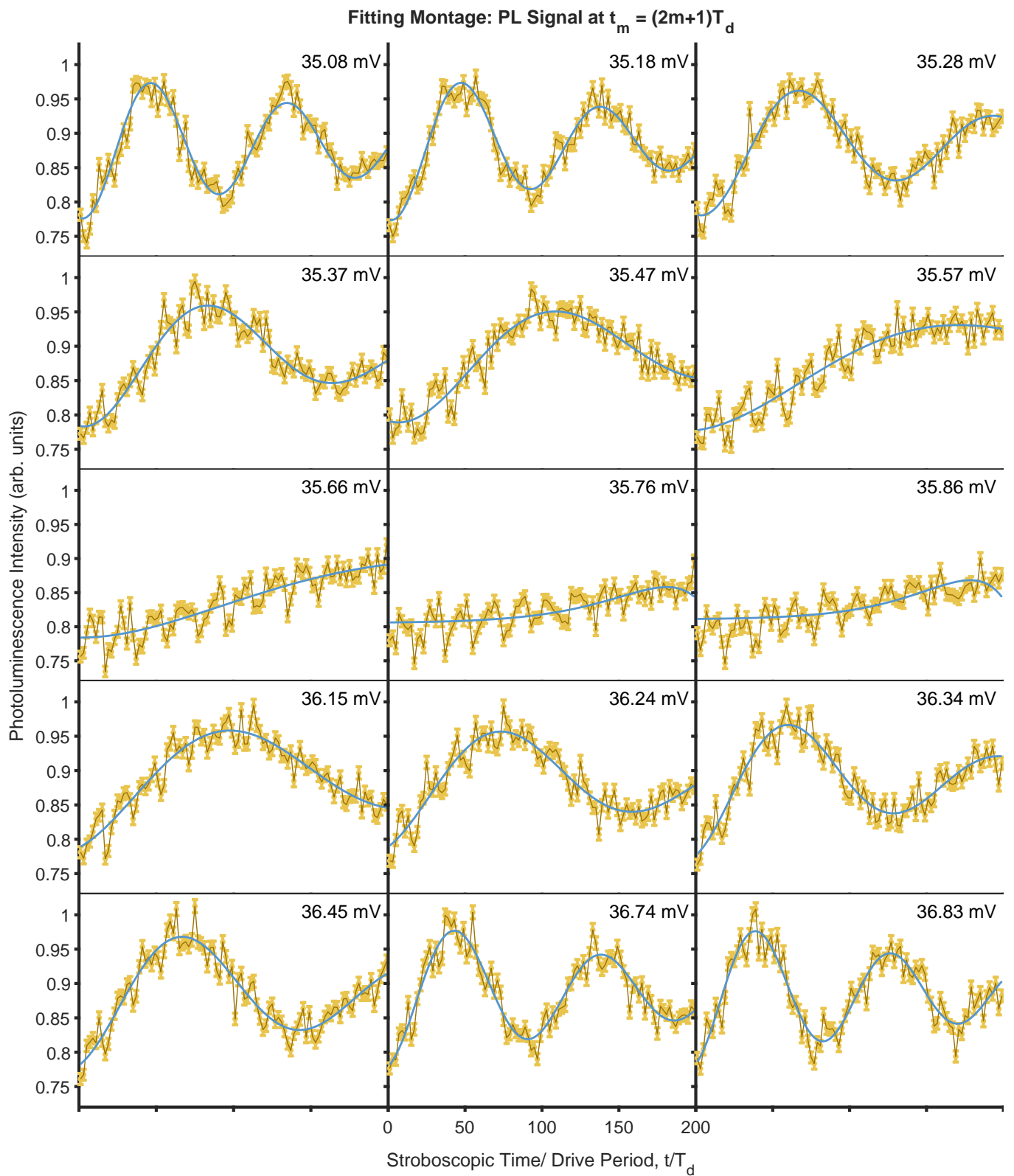


FIG. SI.18. Experimentally obtained PL signal, as depicted in **FIG. 3(a)** (for $t_m = (2m + 1)T_d$), is explicitly plotted (yellow error-bars) for a selection of amplitudes, A_{AWG}/γ , around the period doubling amplitude. The dominant component can be easily extracted as shown by the fitting (blue curves). Additional oscillations about the dominant component correspond to the faint ridges in the DFT shown Fig. SI.17(b).

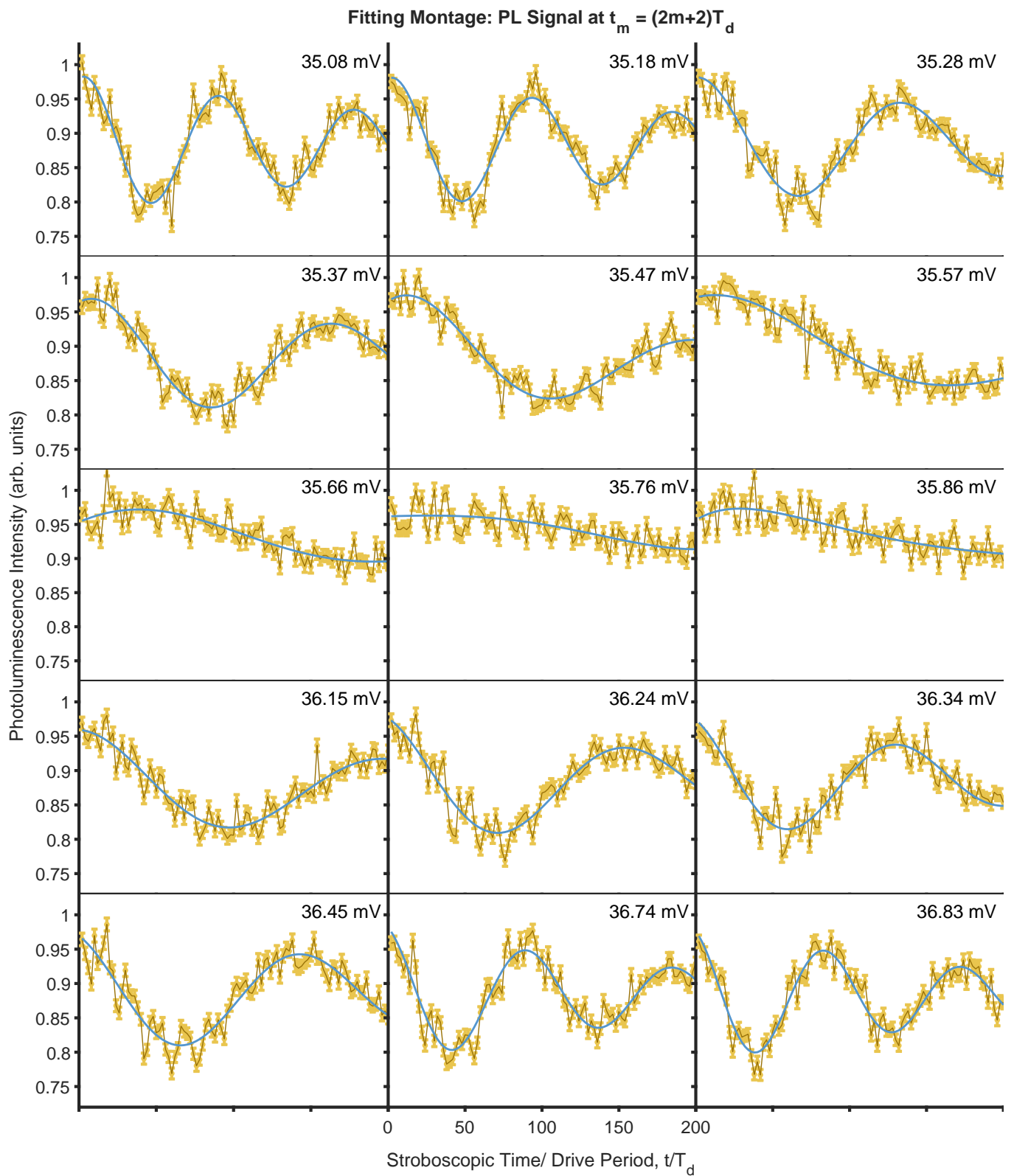


FIG. SI.19. Experimentally obtained PL signal, as depicted in **FIG. 3(a)** (for $t_m = (2m + 2)T_d$), is explicitly plotted (yellow error-bars) for a selection of amplitudes, A_{AWG}/γ , around the period doubling amplitude. The dominant component can be easily extracted as shown by the fitting (blue curves). Additional oscillations about the dominant component correspond to the faint ridges in the DFT shown Fig. SI.17(b).

SI.III: EXPERIMENTAL DETAILS

A. Sample preparation

The diamond sample used in the experiments consists of a 2 mm diameter type IIa electronic-grade single-crystal diamond substrate from ElementSix with (100) face orientation. The substrate was polished into a half-sphere shape to increase collection efficiency. The solid immersion lens geometry enhances the collection efficiency by a factor of 4.4. Subsequently, an isotopically purified (99.999% ^{12}C) layer of approximately 100 nm thickness was grown using a home-built plasma-enhanced chemical vapor deposition (CVD) reactor. Shallow NV centers were then created by ion implantation of $^{15}\text{N}^+$ at a dose of 10^9 cm^{-2} and implantation energies of 5 keV. The diamond samples were subsequently annealed in a home-built UHV furnace at 1000°C for 3 hours to promote the formation of stable nitrogen-vacancy pairs by mobilizing vacancies and to heal radiation damage.

B. Experimental setup

Control of individual nitrogen-vacancy (NV) centers is achieved via fluorescence imaging using a custom-built scanning confocal microscope based on an objective with a numerical aperture of 0.9. The NV centers are optically initialized and read out with a 532 nm laser pulse of $3 \mu\text{s}$ duration, generated by a continuous-wave (CW) laser (Laser Quantum Gem532) and modulated by an acousto-optic modulator (Crystal Technology 3200-146). Pulse sequences—including trigger signals for the laser output and microwave waveforms—are generated using an arbitrary waveform generator (AWG, Tektronix AWG70000A). The radiofrequency (RF) signals are subsequently amplified (Amplifier Research 60S1G4 and Amplifier Research X) and delivered to the NV center via a $20 \mu\text{m}$ diameter copper wire positioned across the diamond sample. Photoluminescence from the NV centers is detected using a single-photon counting module (SPCM, Excelitas SPCMAQRH-4X-TR) and filtered with a 600 nm long-pass filter (Thorlabs FELH0600), which outputs a TTL signal upon photon detection. These TTL pulses are recorded by a multi-event time digitizer (FAST ComTec MCS6A) with a bin width of 3.2 ns. Experimental control and synchronization of all hardware components are managed using the Qudi software suite [24].

C. Experimental procedure

A detailed explanation of the experimental protocol is given below :

1. Create a scanning grid of arbitrary wave generator (AWG) amplitudes, A_{AWG} , to be fed to the RF amplifier. For each of these amplitudes A_i , we will implement the drive sequence mentioned below.
2. Use pulsed-ODMR (optically detected magnetic resonance) technique to determine the resonance frequency and infer the level spacing $\Delta_0(A_i)$ of the transition $|0, 1/2\rangle \rightarrow |+\rangle_\alpha$, before running the drive sequence with amplitude A_i .
3. Compute the drive frequency, $\nu_d \equiv 1/T_d = 1/\Delta_0$.
4. Construct the drive sequence (with drive amplitude A_i) containing pulses of length $T_{\text{pulse}} = nT_d$, with $n = 1, \dots, 200$, as shown in **FIG. 2(b)** of the main text.
5. Implement this drive sequence along with the interspersed measurement sequence as shown in **FIG. 2(b)** of the main text. This gives us the stroboscopically measured PL signal, till time $T_{\text{max}} = 200T_d$, for each amplitude A_i .

Author Contributions– DD composed Sections I and II of the Supplemental Material, which summarize the data analysis and interpretation, incorporating experimental data provided by RBG and RS. RBG and RS compiled Section III, detailing the experimental setup and procedures. All authors were involved in reviewing and editing the final version.